Chapter 4
Physicochemical Characterization of Photocatalytic Materials

Monserrat Bizarro and Sandra E. Rodil

Abstract A wide range of analytical techniques has been employed to obtain the physical–chemical properties of photocatalytic semiconductors prepared as powders or thin films. The photocatalytic activity of a semiconductor material depends on both surface and structural properties. For bulk materials, the composition, crystalline structure, and electronic properties of the materials are intrinsically correlated; however, surface characteristic such as surface area, particle size distribution, and porosity can be independently modified. On the other hand, for nanomaterials, the size becomes an important feature affecting the physical properties, such as the optical band gap. Moreover, the particle size is of primary importance in heterogeneous photocatalysis, because it is directly related to the efficiency of a catalyst through the enhancement of its specific surface area.

The techniques described in this chapter were divided into five major topics: elemental composition, structure and topography, surface area and porosity, and vibrational and optical properties. The most common techniques are briefly described giving some examples about their use for the analysis of a photocatalytic material.

4.1 Elemental Composition

The analytical methods used to measure the composition of solids can be divided in terms of the probe used to analyze the material: ions, electrons, or photons. The spatial resolution for each technique is different and dependent on the instrumentation but also on the type of the detected beam. Some techniques are destructive, while others are nondestructive, as well as surface sensitivity or bulky. This is shown in Table 4.1, where the incident and detected beams are described, as well as the standard spatial resolutions (Egerton 2011).

M. Bizarro (✉) • S.E. Rodil
Instituto de Investigaciones en Materiales, Universidad Nacional Autónoma de México, Circuito Exterior sn Ciudad Universitaria 04510 México D.F., México
e-mail: monserrat@iim.unam.mx

A. Hernández-Ramírez, I. Medina-Ramírez (eds.), *Photocatalytic Semiconductors*,
DOI 10.1007/978-3-319-10999-2_4

Table 4.1 Classification of the analytical characterization techniques in terms of the probe and detected signal

Incident beam	Detected beam	Name	Spatial resolution (nm)	Destructive	Surface sensitive
Ions	Ions	Rutherford backscattering (RBS)	1,000	No	No
		Secondary ion mass spectroscopy (SIMS)	40	Yes	Yes
	Photons	Proton-induced X-ray emission (PIXE)	500	No	Yes
Electrons	Electrons	Electron energy loss spectroscopy (EELS)	<1	No	No
		Auger electron spectroscopy (AES)	2	No	Yes
	Photons	Energy dispersive spectroscopy (EDS)	2–10	No	No
Photons	Photons	X-ray fluorescence spectroscopy (XRF)		No	No
		X-ray absorption spectroscopy (XAS)	20	No	No
	Electrons	Ultraviolet photoelectron spectroscopy (UPS)	1,000	No	Yes
		X-ray photoelectron spectroscopy (XPS)	5–10	No	Yes

4.1.1 Ion Beam Methods

4.1.1.1 Rutherford Backscattering Spectroscopy, RBS

Rutherford backscattering spectroscopy is an ion scattering technique used for the analysis of the surface of solids, and it has become one of the most frequently used techniques for quantitative analysis of composition, thickness, and depth profiles of thin solid films. In RBS a beam of accelerated ions in the MeV range (0.5–4 MeV) impinges on the sample to be analyzed. During the bombardment, a small fraction of the incident particles undergo a direct collision with the nucleus of one of the atoms in the upper few micrometers of the sample. The combination and interplay of three basic concepts allow RBS analysis to detect masses and composition as a function of depth. The first concept is based upon elastic collision of ions with the target nuclei, causing the ions to backscatter and carry information about the mass of the atom they backscatter from. The second concept is the probability of backscattering from different elements, which is highly predictable and proportional to the square of the atomic number, allowing the determination of the sample composition. The third concept is depth analysis, which is possible because backscattered ions are slowed down due to the inelastic energy losses before reaching the surface. The energy measured for a particle backscattering at a given

angle depends upon the material's stopping power and the masses of the projectile to target atoms. The number of backscattering events that occurs for a given element in a sample depends upon two factors: the concentration of the element and the effective size of its nucleus. The probability that a material will cause a collision is called its scattering cross section.

By measuring the heights of the peaks and normalizing them by the scattering cross section for the respective element, the elemental ratio can be obtained at any given depth in the film. Therefore, RBS allows the quantitative determination of the composition of a material without the need of a standard, as well as depth profiling of individual elements with a depth resolution in the nanometer range (Fig. 4.1). Another useful feature of RBS is that it provides an accurate concentration of the total atoms/cm^2, which is present in a film. If the thickness of the film can be measured by another method, then the density of the film can be easily calculated (Tesmer and Nastasi 1995).

4.1.1.2 Elastic Recoil Detection Analysis, ERDA

RBS has a very good sensitivity for heavy elements in the ppm range but is not sensitive to light masses. In order to determine the heavy and the light components of a matrix, RBS and elastic recoil detection analysis (ERDA) are used simultaneously. ERDA uses the same incident beam as RBS but detects the energy of the recoiled atoms. An absorber foil prevents scattered particles from the sample entering the detector. As a result, only the lighter recoiled particles (hydrogen or deuterium) will be measured (Tesmer and Nastasi 1995). Nowadays, a new configuration has been designed, heavy incident ion-ERDA (HI-ERDA), where heavier ions are used (^{35}Cl, ^{63}Cu, ^{127}I, and ^{197}Au). This configuration coupled with elemental mass-sensitive detectors allows the identification of all atoms from the target sample with masses lighter than the projectile ion. No absorber is used in this case, but the recoiled projectile can be also identified. The most common detectors are magnetic spectrographs, gas ionization detectors, or time-of-flight-ERDA (TOF-ERDA); in the latter the elements are identified by the simultaneous detection of velocity and energy (Siketic et al. 2010). A great improvement has been obtained in terms of depth resolution, which is in the 1–2 nm range, allowing depth profile analysis with high precision and atomic resolution better than 0.1 at.% (Schiettekatte and Chicoine 2004).

4.1.1.3 Particle-Induced X-Ray Emission or Proton-Induced X-Ray Emission PIXE

In PIXE, the elemental composition is obtained by measuring the energy of the X-rays emitted by the sample after bombardment with energetic ions. Since the incident protons (typically of energy 1–5 MeV) are only slightly deflected by the nuclear field, the bremsstrahlung background radiation characteristic of the

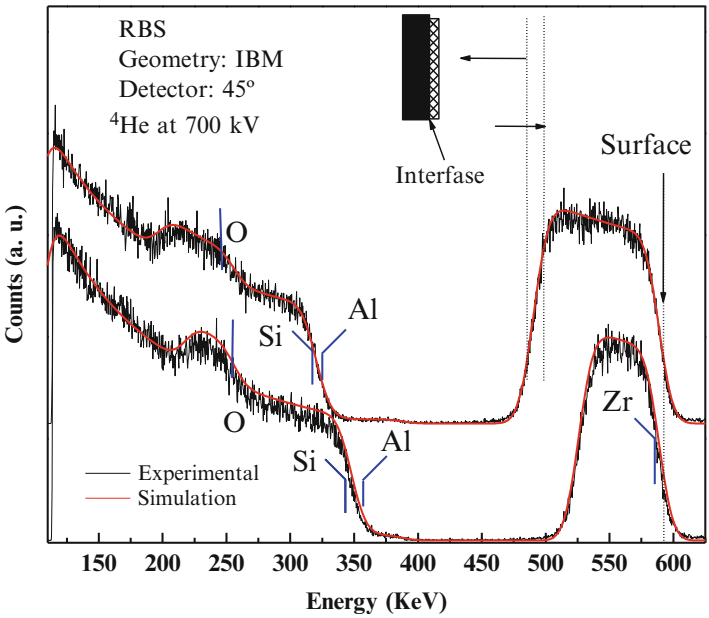

Fig. 4.1 Example of an RBS spectra for Al-doped ZrO_2 thin-film samples having different thicknesses. The ions used are indicated, as well as the specific sample–detector geometry (IBM)

X-ray peaks is lower than when using incident electrons, and then sensitivities as low as 0.1–10 ppm can be attained. Besides, the spatial resolution can be improved up to 1 μm using tightly focused ion beams (Johansson et al. 1995).

4.1.1.4 Secondary Ion Mass Spectrometry, SIMS

In SIMS, the sample is bombarded with a focused ion beam 1–20 keV ions (O^{2+}, O^-, Cs^+, Ar^+, Ga^+, or neutrals); this causes the sputtering of surface atoms (secondary ions), whose mass/energy ratio are analyzed by passing them through a mass spectrometer. The mass analyzer may be quadrupole mass analyzers or magnetic sector mass analyzers, and more recently, time-of-flight (TOF) analyzers have been used providing substantially higher sensitivity and mass resolution, as well as a much greater mass range. The secondary ions come from a surface layer of 1–2 nm thick; typically one monolayer is analyzed in static mode SIMS, while in dynamic mode, bulk composition and depth distribution of trace elements are investigated with a depth resolution ranging from sub-nanometer to tens of nanometer. One example of the profile composition for light elements from a thin film (amorphous hydrogenated carbon nitride) deposited on silicon is shown in Fig. 4.2. All elements from hydrogen to above are detectable, and the technique is capable of detecting impurity elements present in a surface layer at <1 ppm concentration and bulk concentrations of impurities of around 1 ppb. Moreover, chemical images are

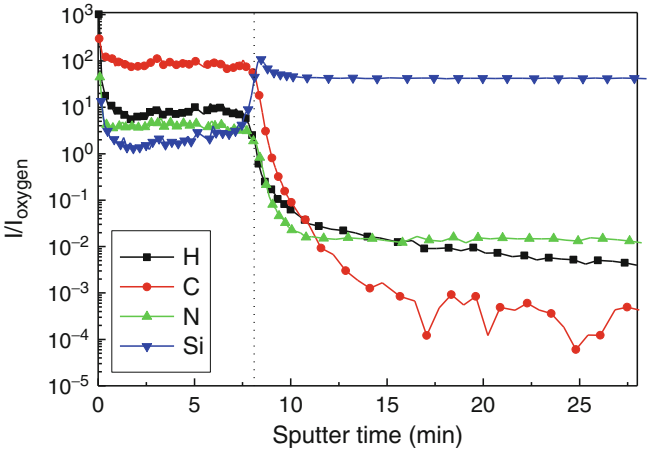

Fig. 4.2 Example of a depth profile for a hydrogenated carbon nitride thin film deposited on a silicon substrate. Note the clear change in the composition at the film–substrate interface

possible by collecting a mass spectrum at every pixel as the primary ion beam is scanned across the sample surface. However, quantification in SIMS is complicated by the fact that sputtering gives rise to both neutral atoms and ions, but most of the spectrometers detect only the ions. Therefore, for quantitative analysis it is necessary to use standard samples with similar matrix composition. The flux of sputtered ions is very low and strongly depends on the surface composition (matrix effects). While the probability of sputtering neutral atoms is much higher (90–99.9999 %) and less sensitive to the surface composition, its detection allows a much better quantitative estimation of the sample stoichiometry. This has led to the design of a different method of detection for a better quantification, namely, secondary neutral mass spectroscopy SNMS, that ionizes the neutral atoms (by an electron gun, laser, or radio-frequency cavity) before detection (Briggs and Sheah 1996).

4.1.2 Electron Beam Methods

In this group, we consider all those techniques where the elemental composition can be obtained by analyzing the interaction of an electron beam with core electrons; such interactions bring information about the binding energy of the core electrons, and then the elemental composition as well as the chemical bonding and electronic structure of the material can be obtained. The most common techniques are Auger electron spectroscopy (AES), electron energy loss spectroscopy (EELS) and X-ray emission spectroscopy, most commonly known as energy dispersive X-ray spectroscopy (EDX) or electron probe microscopy analysis (EPMA). The fundamental physical phenomena used to estimate the chemical composition for the different techniques are schematically shown in Fig. 4.3.

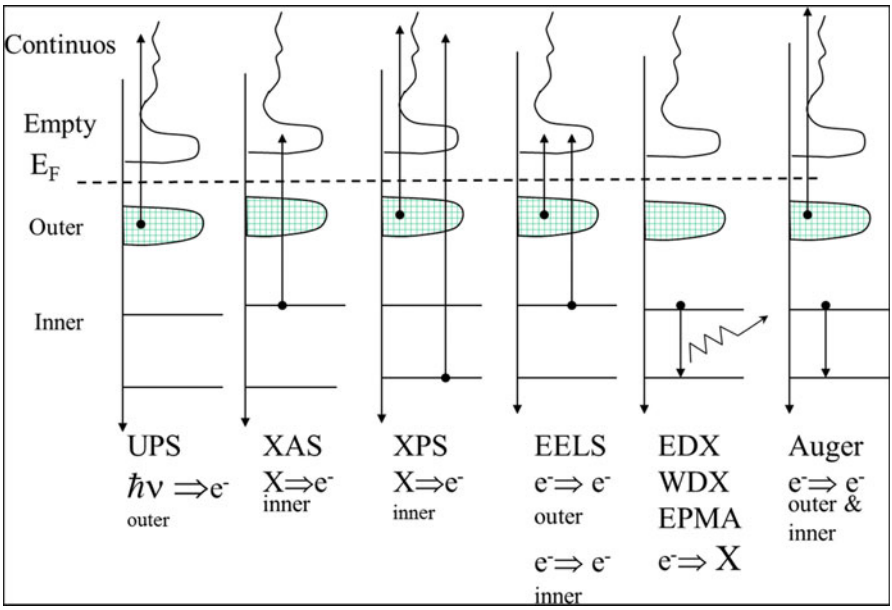

Fig. 4.3 Schematic representation of the electronic transitions and the de-excitation mechanisms used for the chemical characterization of solid

The energy of the incoming electrons have to be large enough to remove one electron from a core level, leaving a hole in the energy level, which is later filled through a decay mechanism, such as the emission of an X-ray (EDX) or the emission of a secondary electron (AES), where the energy of the emitted beam is directly measured and correlated to the corresponding energy level. Meanwhile in EELS, the energy loss suffered by the incident electron due to the interaction with the core electrons is measured.

4.1.2.1 X-Ray Emission Spectroscopy, XES

As its name indicates, in this technique the energy of X-rays emitted by the sample after interaction with a beam of energetic electrons is measured (Goldstein et al. 2003). The energy or wavelength of the emitted X-rays is analyzed using either a wavelength spectrometer (WDX) or an energy spectrometer (EDX). The resolution of the WDX is much larger (10 eV), allowing a better identification of the elements; however, the acquisition time is much larger than using energy spectrometers (130 eV energy resolution). As a method of elemental bulk analysis, the technique is known as EPMA, and it has been improved to give elemental accuracy of about 1–2 % using appropriate standards and corrections for atomic number, absorption, and fluorescence effects. On the other hand, EDX has been attached to either transmission or scanning electron microscopes, leading to a high spatial

resolution. In any case, no H or He can be detected, and detection of light elements (B, C, N, O) within heavy element matrices is always controversial, since the probability of excitation decay by X-ray emission is much lower for the light elements. Moreover, in order to keep the required vacuum in the microscope column, a window between the chamber and the detector has to be used, which filters the low energy photons. Windowless equipment allows the detection and quantification of elements above boron at high sensitivity with detection limits between 0.01 and 0.1 %. One interesting feature that has been extensively improved in the last years is the X-ray mapping, where nanometric segregations of certain compounds or elements within the matrix can be easily detected. EDX is nowadays the most common technique used to analyze the composition of bulk samples. It is important to consider that it is not a surface science technique, since the X-rays are generated in a region about 2 μm in depth and quantitative analysis is mainly done by software, instead of using appropriate standard samples.

4.1.2.2 Electron Energy Loss Spectroscopy, EELS

Electron energy loss spectroscopy is another microanalytical technique used to obtain information about the elemental and chemical composition, as well as the electronic structure of materials. However, since EELS measures the energy loss of transmitted electrons, it has to be coupled to a transmission or scanning transmission electron microscope. It has very good spatial resolution (0.1–1 nm) but requires very thin samples, either nanoparticles or thin films (<50 nm). Imaging is also possible, providing the highest resolution compositional maps.

The loss spectroscopy consists of the analysis of the energy distribution of initially monoenergetic electrons that have interacted inelastically with the specimen. Provided the incident energy is high enough and the film sufficiently thin, practically all of the incident electrons are transmitted without reflection or absorption. The elastic and inelastic processes occurring when electrons bombard solid samples are shown in Fig. 4.4. Inelastic interaction with core electrons takes place inside the specimen, and information about internal structure can be obtained by passing the transmitted beam into a spectrometer (Egerton 2011).

Energy loss implies inelastic collision but the spectrum will also contain electrons that have interacted elastically with the specimen (Froitzheim 1977). Thus, the EELS spectra consist of three principal regions, as shown in Fig. 4.5:

- The zero-loss region consists primarily of elastic forward scattered electrons but also contains electrons that have suffered minor (unresolvable) energy losses.
- The low-loss region up to an energy loss of ~50 eV contains electrons which have interacted with the weakly bound outer-shell electrons of the atoms in the specimen or by the excitation of vibrational transitions. Such low energy losses can be detected in high-resolution EELS, which is used to study the adsorption of molecules on surfaces.

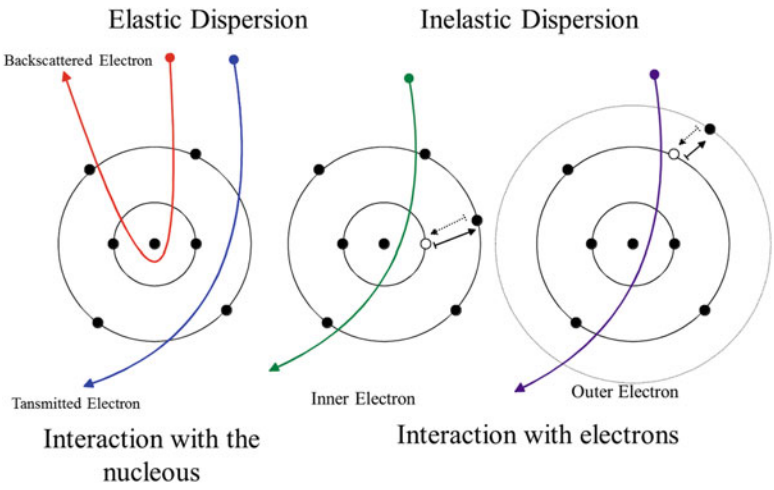

Fig. 4.4 Representation of the inelastic and elastic interaction of the incidence electrons with the atoms of a solid sample

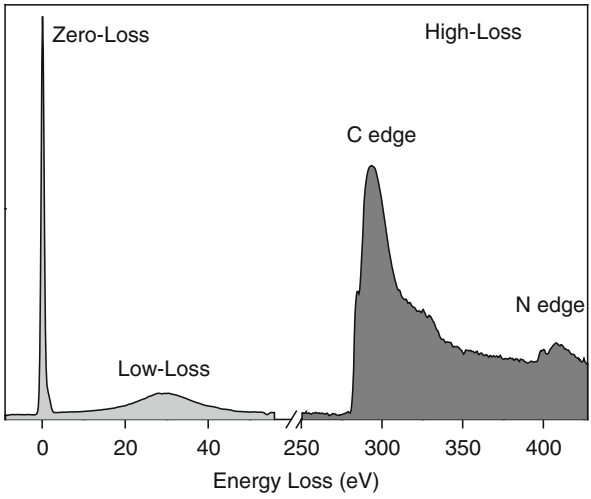

Fig. 4.5 Typical energy loss spectra, after background subtraction and plural scattering removal, where C and N edges are observed in the high-loss region

- The high-loss region contains electrons that have interacted with the more tightly bound inner-shell or "core" electrons.

Each region gives different information; the zero-loss peak defines the energy resolution and is used to calibrate the energy scale of the spectrum.

The low-loss region is due to inelastic interaction between the incident electrons and the outer-shell electrons of the specimen. There are two types of interactions, single electron excitation in which a valence electron makes an interband transition across the energy gap for a semiconductor or in the case of a metal a conduction

electron makes a transition to a higher state within the same energy band. The analysis of this part of the spectra allows the determination of the optical band gap and its character, as well as inter-intraband transitions. The other interaction is a collective electron excitation in which the scattering involves many atoms of a solid. This collective effect is known as a plasma resonance and takes the form of a longitudinal traveling wave. The excitation can also be described in terms of the creation of a pseudoparticle, the plasmon, whose energy is given by $E_p = \hbar w_p$, where w_p is the frequency (rad/s) that is proportional to the square root of the valence electron density, as shown in Eq. (4.1):

$$E_p = \hbar \left(\frac{n_e e^2}{\varepsilon_o m^*} \right)^{1/2} \tag{4.1}$$

where e and m^* are the electron charge and effective mass, ε_o is the permittivity of free space, and n_e is the valence electron density. Even though E_p is proportional to the density of free electrons, there are also plasmon-like spectra from insulator materials. A simple explanation for the occurrence of plasmon effects in insulators is that electrons that receive energy in excess of their binding energy are released to take part in collective oscillations. Thus, analysis of the low-loss region can provide information about the inter-intraband transitions, optical gap, and surface and bulk plasmons of the sample.

The high-loss regions comprised the chemical information, composition and chemical bonding. When the beam of electrons transfer more energy than the attractive fields of the nucleus to K, L, M, N, or O shell electrons, the electrons are transferred to an unoccupied electron state. Because the total energy is conserved at each collision, the fast incident electron loses an amount of energy comparable to or greater than the core electron binding energy. A specific minimum energy transfer is required to overcome the binding energy of the electron to the nucleus and ionize the atom. This minimum energy constitutes the ionization threshold E_c characteristic of the given inner shell (K, L, or M). The ionization loss electrons have an energy distribution that ideally shows a sharp rise to a maximum E_c, followed by a slowly decreasing intensity above E_c back toward the background due to electrons that have undergone random plural inelastic scattering events (steplike peaks). The edge may also contain fine structure around E_c that is due to the bonding effects, and its analysis is termed electron loss near edge structure (ELNES). More than ~50 eV after the edge, small intensity oscillations may be detectable due to diffraction effects from the atoms surrounding the ionized atoms (extended energy loss fine structure, EXELFS).

Therefore, elemental analysis by EELS is enabled by the inner-shell edges. The position and intensity of which can be used to identify and quantify atomic species within the sample, while the analysis of the fine structure gives information about the chemical bonding (π, σ bonding character), most suitable for atoms with $Z < 33$. The quantification of the EEL spectra requires the knowledge of the partial scattering cross section, i.e., differential cross section integrated over angle and energy.

This cross section can be determined either theoretically or experimentally by using standards. Such calculation and the lack of extended databases have limited the use of the technique as a widespread characterization tool (Keast et al. 2001).

4.1.2.3 Auger Electron Spectroscopy, AES

Auger spectroscopy owns its name to Pierre Auger, who discovered that the emission of a lower binding energy electron was also a relaxation process after the ionization of a core electron by the bombardment with electrons or photons with enough energy. For AES, electrons of energy 3–20 keV are incident upon a conducting sample. These electrons cause core electrons from atoms contained in the sample to be ejected resulting in a photoelectron and an atom with a core hole. The atom then relaxes by the transition of an electron with a lower binding energy dropping into the core hole. The energy thus released can be converted into an X-ray (as in EDX) or emit an Auger electron (Fig. 4.6). After the emission of the Auger electron, the atom is left in a doubly ionized state, and the energy of the Auger electron is characteristic of the element that emitted it and can thus be used to identify the element (Davis 1996; Briggs and Sheah 1990).

The short inelastic mean free path (IMFP) of Auger electrons in solids ensures the surface sensitivity of AES. For the Auger process, there are always three energy levels involved with well-defined selection rules for the transition, allowing elemental identification. The energy level of the core hole will often determine which transition types will be favored. For single energy levels, i.e., K, transitions can occur from the L levels, giving rise to strong KLL type peaks in an Auger spectrum. Higher level transitions can also occur but are less probable. For other shells, transitions are available from higher energy orbital, such as LMM and LLM. As the atomic number Z increases, so does the number of potential Auger transitions. Fortunately, the strongest electron–electron interactions are between levels that are close together, giving rise to characteristic peaks in an Auger spectrum of the KLL and LMM type. Quantitative analysis is possible by the use of standards or relying on Auger databases (semiquantitative) where the yield of Auger electrons has been reported for different elements. The depth analysis of AES is of a few nanometers, 2–5 nm, and can detect elements from Li and onward in the periodic table. Due to the possibility of focusing the incoming electrons, it has a better spatial resolution (10 nm) than XPS, so the analyzed area becomes more specific. The acquisition of Auger spectra has changed in the last years due to the improved sensitivity of the electron analyzers. During the initial years, derivative spectra were obtained to enhance the small signals, but nowadays direct spectra can be acquired and this has changed the method to analyze AES data. Chemical imaging is also possible taking advantage of the focused electron beam, which can be scanned on the surface; this has been named as scanning Auger microscopy (SAM). The major limitation of AES is that the surface of the sample is charged, which leads to peak shifting and loss of resolution, and so conductive samples have to be used or a secondary process has to be implemented to avoid charging effects. Note that the Auger signals can

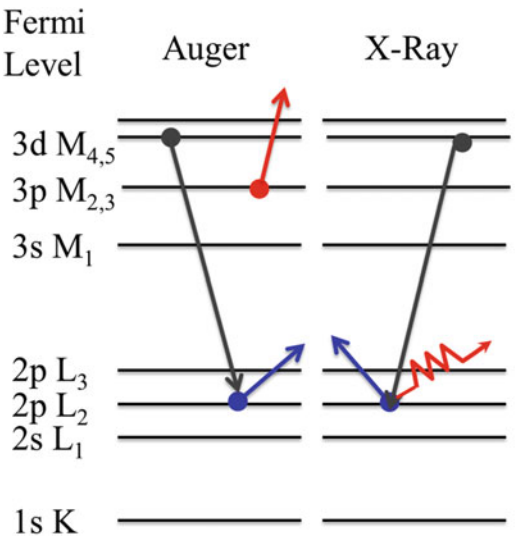

Fig. 4.6 Schematic representation of the energy levels involved in an Auger event in comparison to X-ray emission

also be detected in any of the other analytical techniques, when the electrons constitute the detected beam, as in the XPS or NEXAFS.

4.1.3 X-Ray Beam Methods

Another group of elemental composition techniques use photons as the incident beam. The energy of the photons (X-ray range) has to be enough to cause ionization of the inner or core-shell electrons, and the emitted electrons (XPS) or photons (XAS) are detected.

4.1.3.1 X-Ray Photoelectron Spectroscopy, XPS

The phenomenon used for photoelectron spectroscopy is based on the photoelectric effect outlined by Einstein where the concept of the photon was used to describe the ejection of electrons from a surface when photons impinge upon it.

For XPS, also known as electron spectroscopy for chemical analysis (ESCA), the photon energies of choice are the fundamental emissions from Al-κα (1,486.6 eV) or Mg-κα (1,253.6 eV) cathodes. The XPS technique is highly surface specific due to the short IMFP of the photoelectrons that are excited from the solid. The energy of the photoelectrons leaving the sample is characteristic of each element.

Each peak area is proportional to the number of atoms being present in the material; the shape of the peak and the binding energy (BE) can be slightly altered by the chemical site of the emitting atom; hence XPS can provide chemical bonding

information as well. The fundamental equation that relates the BE of the emitted photoelectron with the measured electron kinetic energy (KE) is given by

$$\mathrm{BE} = h\nu - \mathrm{KE} - \phi \tag{4.2}$$

where ($h\nu$) is the incident photon energy and (ϕ) is the work function, which has to be well defined for each equipment in order to determine precisely the BE that is usually measured in reference to the material's Fermi level.

The analysis of the XPS spectrum (counts per binding energy) allows us to obtain the surface elemental composition by comparing to standard materials (quantitative) or using XPS databases (semiquantitative). The depth of analysis in XPS is about 1–10 nm depending on the incidence energy of the photons, the kinetic energy of the outgoing electrons, and the angle of collection (angle resolved XPS, ARPES). The XPS technique requires ultra-high vacuum conditions (UHV, pressure in a range from 10^{-8} to 10^{-10} mbar), and so the samples have to be evaluated always in dry conditions. The XPS is essentially a nondestructive technique but is very sensitive to surface contamination; so in some cases, an in situ cleaning process is applied using an ion gun (Watts and Wolstenholme 2003; Briggs and Sheah 1990).

4.1.3.2 X-Ray Absorption Spectroscopy, XAS

Absorption of X-rays by a solid sample can also give information about the chemical composition and structure of the sample (Bunker 2010). X-ray absorption includes different techniques: near edge X-ray fine structure (NEXAFS), X-ray absorption near edge structure (XANES), and extended X-ray absorption fine structure (EXAFS), schematically shown in Fig. 4.7. The term NEXAFS is typically used for soft X-ray absorption spectra (Stohr 2003), where the edge (similar to EELS) corresponding to elemental absorption is observed, whereas XANES is used for hard X-ray spectra and EXAFS refers to the analysis of the oscillations due to the interaction of the electron wave with the rest of the atoms in the sample. In general, a monochromatic X-ray beam is directed at the sample, and the photon energy of the X-rays is gradually increased. Below the absorption edge, the photons cannot excite the electrons of the relevant atomic level, and thus absorption is low. However, when the photon energy is sufficient to excite the core electrons into empty states, then a large increase in absorption occurs, known as the absorption edge. A few electron volts above the absorption edge, the spectra shows a series of oscillations due to interaction of the outcoming photoelectrons with the atoms surrounding the emitting atom, but also because the probability of backscattering is dependent on both the energy of the photoelectrons and the photon energy. These oscillations can be used to determine the atomic number, distance, and coordination number of the atoms surrounding the element whose absorption edge is being examined. The necessity to sweep the photon energy (200–35,000 eV) requires the use of synchrotron radiation.

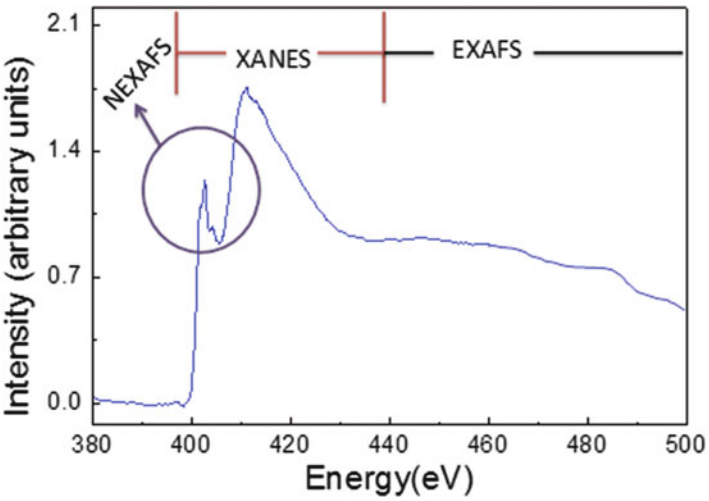

Fig. 4.7 Schematic representation of X-ray absorption spectra showing the different region of analysis

In NEXAFS, the X-ray energy is scanned and the absorbed X-ray intensity is measured, by detecting the emitted photoelectrons, the Auger electrons, or the fluorescent photons. NEXAFS is very sensitive to the surface, and it is particularly important to study chemisorbed molecules on surfaces. For XANES experiments, analysis of the near edge region (up to 40 eV above the edge) can provide information about vacant orbitals, electronic configuration, and site symmetry of the absorbing atom. The absolute position of the edge contains information about the oxidation state of the absorbing atom. These techniques are very sensitive to directional bonds by the use of linearly polarized X-rays and therefore are well suited for covalent systems like low-*Z* molecules, macromolecules, and polymers (Haw 2002).

4.1.4 Examples

One interesting example where different analytical techniques were used to understand the electronic–catalytic response of ceria-doped titania samples is given by Kundu et al. (2012). The interest about Ce–TiO_2 comes from theoretical calculations done by Catlow et al. (2010) that suggest that the presence of reduced cerium cations will enhance the photocatalytic activity of TiO_2. However, none of the reported works (Li et al. 2009; Xie et al. 2010) have investigated the oxidation states of the cerium. For such purpose, the authors (Kundu et al. 2012) produced Ce-modified TiO_2 samples by wet impregnation of TiO_2 using two different Ce concentrations: 6 and 15 wt %. Then, HRTEM, EELS, NEXAFS, and XANES were

used to determine the oxidation state of the cerium and their structural distribution. The HRTEM images showed that CeO_2 particles were generally located at a TiO_2 corner site, and they have a truncated pyramidal shape. Electron energy loss spectroscopy was employed to measure the Ce^{3+}/Ce^{4+} ratio with high spatial resolution within and around the ceria nanoparticles. The presence of Ce^{3+} was observed mainly at the CeO_2–TiO_2 interface, as indicated by the NEXAFS forming a mixed oxide at the interface. The XANES spectra showed that the incorporation of the CeO_2 onto the TiO_2 surface changed the charge transfer between oxygen and Ce, probably due to a Ce–O–Ti interaction. The authors also analyze the $Pt/CeO_2/TiO_2$ systems showing that without the presence of Pt, the pure CeO_2/TiO_2 mixed metal oxide showed a very small activity toward water splitting in the visible light. This result indicates that the existence of Ce^{3+} drastically enhances the formation of electron–hole pairs, but it does not help to suppress their recombination. The presence of a small amount of Pt is needed in order to act as an electron trap and prolong the lifetime of electron–hole pairs. However in this particular system, Pt not only acts as an electron-trapping center, but also increases the amount of Ce^{3+} in the support itself, thus enhancing the photon absorption efficiency of the catalyst in the visible region.

McDermott et al. (2013) have used a combination of X-ray absorption and electron energy loss spectroscopies along with theoretical calculations to investigate the electronic structure of poly(triazine imine) (PTI), a graphitic carbon nitride-type material with LiCl intercalation. The PTl/LiCl is aimed to improve the water-splitting photocatalytic reaction, since Li and Cl ions can donate or withdraw charge from the polymeric matrix. It was observed that the addition of LiCl reduced the band gap ($\sim$2.2 eV) with respect to polymeric carbon nitride (2.7 eV).

Qi et al. (2012) have produced transition metal-doped TiO_2 transparent sols via a simple chemical route. The sol samples were analyzed using HRTEM, XRD, EELS, and XPS, verifying that most metal ions have been doped with TiO_2 forming Ti–O–metal bonds. Analyses of XRD, EELS, and XPS experiments allow them to verify that most of the dopant metal ions substitute the Ti^{4+} sites, forming metal-doped TiO_2 sols instead of just mechanically mixed phases. These doped TiO_2 sols exhibited good photocatalytic activities under visible light irradiation and were stable in sealed conditions for several months without formation of precipitates.

Oxide supported noble metal systems have been studied intensively due to their extreme importance in catalysis; therefore, gathering information about the interface of the noble metal with the support is always of great interest, but not easily done. Wang et al. (2013) prepared thin iron oxide films of FeO(111), Fe_3O_4(111), and Fe_2O_3(0001) on Mo(110) substrate. The growth and electronic structures of silver on these films with different morphologies were investigated by using various surface analytical techniques including low energy electron diffraction (LEED), AES, UPS, and EELS. The analysis of the valence band structure and surface plasmons showed that silver grows on FeO(111) and Fe_2O_3(0001) as three-dimensional (3D) clusters but forms a wetting layer on Fe_3O_4(111). This difference

on growth will have an impact of the photocatalytic response of the noble metal–iron oxide system, although it was not evaluated in the paper.

Nitrogen doping of TiO_2 samples has been extensively investigated as a method to enhance the photocatalytic effect of TiO_2 under visible or white light irradiation. However, it is not trivial to detect nitrogen at very low levels in order to determine the doping characteristics. Doping concentrations as low as 1.19 at.% were shown by Tavares et al. (2009) to improve the photocatalytic degradation of an organic dye by TiO_2-anatase films deposited by RF magnetron sputtering. Such low concentration levels were accurately determined using HI-ERDA. The effect of nitrogen and sulfur doping in commercial TiO_2 powders was also investigated by Rengifo-Herrera et al. (2008), where a careful analysis of the XPS peak assignments for both N and S was presented. The authors were able to identify the type of doping, interstitial or substitutional, through XPS analysis, a subject that is important to understand the energy position of the gap level states introduced in the structure by the dopants. Sério et al. (2012) used RBS and ERDA to study the effect of the nitrogen doping on the growth, structure, crystallinity, and optical properties of TiO_2 thin films deposited by DC-reactive magnetron sputtering. Similarly, Moser et al. (2013) studied the effect of N and C doping on TiO_2 films and demonstrated that the high activity of the films was associated to the presence of N and C acting as dopants, which increases the absorption in the near-UV region. The dopant level was demonstrated by RBS, ERDA, and XPS.

4.2 Structure and Topography

4.2.1 Structure

The photocatalytic activity of semiconductor materials mainly depends on its intrinsic properties, such as the composition and crystalline structure. In this regard, it is important to know the active crystalline phase or mixture of phases in the photocatalyst. The most important techniques used to identify the crystalline phases in materials are X-ray diffraction (XRD) and transmission electron microscopy (TEM).

4.2.1.1 X-Ray Diffraction, XRD

X-ray diffraction involves the measurement of the intensity of X-rays scattered from crystals. Waves scattered at atoms at different positions arrive at the detector with a relative phase shift, producing constructive and destructive interference patterns depending on the angle and the relative atomic positions (Suryanarayana and Norton 1998; Waseda et al. 2011). The easiest access to the structural

information in crystals is using the Bragg equation, which describes the principle of X-ray diffraction in terms of a reflection of X-rays by sets of lattice planes:

$$n\lambda = 2d \sin\theta \tag{4.3}$$

where n is called the order of diffraction and is equal to the number of wavelengths in the path difference between rays scattered by adjacent planes, λ is the wavelength of the incident photon, d is the interplanar distance, and θ is the diffraction angle.

Lattice planes are crystallographic planes, characterized by the index triplet (hkl), the so-called Miller indices. Parallel planes have the same indices and are equally spaced, separated by the distance d_{hkl}. Bragg analysis treats the X-rays as a mirror-like reflection at the lattice planes. As the X-rays penetrate deep inside the material, multiple reflections occur at thousands of consecutive parallel planes.

For an infinite stack of lattice planes, Bragg's equation gives the position of delta-function Bragg peaks. In practice, finite size crystallites give rise to Bragg peaks of finite width. This size broadening is described by the Scherrer equation given by

$$L_{hkl} = \frac{K\lambda}{\beta_{hkl} \cos\theta} \tag{4.4}$$

where K depends on the shape of the grains; for perfect spheres $K = 0.89$, and $K = 0.94$ for cubic shaped grains. Besides the size broadening of the diffraction peaks described by the Scherrer equation, the width is also affected by other microstructural features like the crystallite shape, the shape distribution, and any distortion of the crystal structure like microstrain, dislocations, twin planes, and stacking faults.

The X-ray diffraction technique is a powerful nondestructive tool for phase identification of crystalline samples. Unlike other techniques to obtain the chemical composition, XRD does not give elemental composition but can distinguish different packing ways of the same set of elements. In the case of TiO_2, it is known that it is composed of titanium and oxygen atoms, but XRD allows determining the crystalline arrangement in which they are disposed. In the case of TiO_2 we can find a tetragonal structure (anatase or rutile) or even an orthorhombic structure (brookite), as shown in Fig. 4.8 for P25 Degussa TiO_2 particles.

Interpretation of XRD patterns have become easy due to the large amount of crystalline structures that have been already identified and classified into proper databases (more than 50,000 validated patterns for inorganic materials). Nevertheless for unknown materials, the interpretation is rather more complicated. Fortunately, about 45 years ago, Rietveld (1969) provides us with a quantitative tool to analyze the X-ray powder diffraction patterns, known as the Rietveld method (RM). The Rietveld method is a standard-less method that allows the accurate determination of a wide range of structural parameters. It is a computing-demanding method, and different open-source or commercial software have been developed. The most common information obtained is:

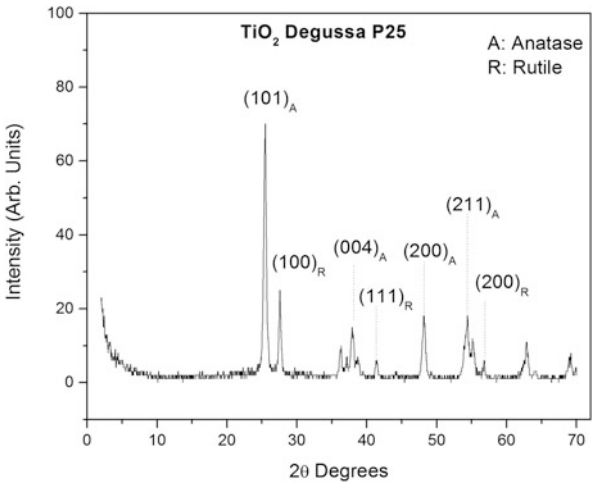

Fig. 4.8 XRD pattern for standard P25 TiO_2 particles (Degussa) showing the two crystalline phases: anatase and rutile

- Quantitative determination of the percentage of different phases present in one sample (quantitative phase analysis) (Gualtieri 2000)
- Percentage of crystallinity or amount of disorder (Chipera and Bish 2013)
- Atomic resolution for solid solution materials
- Unit cell determination
- Crystalline size
- Global residual stress.

Therefore, the percentage of anatase and rutile in the XRD pattern shown in Fig. 4.8 could be accurately determined by a Rietveld refinement of the structure. On the other hand, for the calculation of this fraction where only two polymorphs are present, semiquantitative methods can also be applied. In such case, the integrated intensity of the strongest peak for each phase is compared to the integrated intensity of the pure phase (Guillén et al. 2014). However, such calculations are prompt to errors due to the presence of not identified phases, overlapping peaks, or preferred orientation of individual phases. An alternative quantitative method that is more precise is the matrix flushing method or normalized RIR (Reference Intensity Ratio) method (Chung 1974). In this case, a least square fitting of the full experimental pattern is performed to identify the phases present in the mixture. Then, the weight fraction of each phase can be determined using the RIR values commonly listed in the databases such as the ICDD. The RIR values contain the intensity ratio between the target material/phase and a known standard, usually corundum. However, there is some criticism about the use of the RIR method, and other methods combining both RIR and Rietveld methods have also been proposed (Chipera and Bish 2002, 2013).

Different modes have been attached to the XRD systems; the most commonly used is the Bragg–Brentano (BB) configuration suitable for powders and polycrystalline bulk samples. In the BB mode, the penetration depth of the X-rays is often found in the 10–100 μm range, causing than when thin films (less than 1 μm thick)

are studied, the substrate peaks dominate the pattern. Thus, for the analysis of thin films, X-ray diffraction techniques have been developed for which the primary beam enters the sample under very small angles of incidence. In its simplest variant this configuration is denoted by GIXRD that stands for grazing incidence X-ray diffraction (Ulyanenkov 1998). More recently, the In-Plane mode has been introduced to study the crystal structure of very thin films in the direction perpendicular to the substrate. Information about the texture, i.e., preferred crystallographic orientations in thin films and polycrystalline samples, can also be obtained by XRD using a mode called XRD Pole figures. In thin films, it is common that a certain crystallographic direction (*hkl*) is preferentially oriented with respect to the sample reference frame (powders) due to the directional growth. This anisotropy of crystallite orientation has important effects on different physical properties of both the thin films and polycrystals, such as oxidation, diffusion of atoms, phase transformations, as well as mechanical, electrical, and magnetic properties.

Other interesting variation of the XRD technique is the small angle X-ray scattering (SAXS) configuration (Glatter and Kratky 1982), which is typically done using synchrotron radiation or dedicated SAXS equipment, but recently has been also incorporated into standard XRD systems (GISAXS). This is a very powerful technique for the structural characterization of nanomaterials and surfaces. In this configuration the sample is irradiated with a monochromatic X-ray beam at very low angles, typically 0.1–10°. This angular range contains information about the shape and size distribution of nanoparticles (1–100 nm), characteristic distances of partially ordered materials, pore sizes, and other data. SAXS is capable of delivering structural information of macromolecules between 5 and 25 nm, of repeat distances in partially ordered systems of up to 150 nm.

4.2.1.2 Transmission Electron Microscopy, TEM

The transmission electron microscope uses a high energy electron beam that is transmitted through a very thin sample to image and analyze the microstructure of materials with atomic scale resolution (Williams and Carter 1996; Reimer and Kohl 2008). The TEM is an electron–electron technique; the incident electrons are accelerated at high voltages (100–1,000 kV) to a velocity approaching the speed of light (0.6–0.9*c*). The electrons travel through the sample suffering both elastic and inelastic dispersion (as shown in Fig. 4.3). The elastically dispersed electrons are used to form a diffraction pattern which follows the Bragg law and therefore contains information about the crystalline structure. Meanwhile, the inelastically dispersed electrons are those typically detected in the EELS experiments described above. High-resolution TEM images are formed focusing the transmitted electrons to a plane where both the CCD camera and/or the fluorescence screen are placed; there the electron density is converted into light-optical images. The great advantage in imaging microscopy is that the associated wavelengths are five orders of magnitude smaller than the visible light wavelength, about 0.04–0.008 Å,

depending on the voltage of acceleration. This would mean a nearly infinite resolution. However, the resolution is limited by aberrations inherent to the electromagnetic lenses, to about 1–2 Å. Nevertheless this is good enough to obtain nanometric imaging and structure determination at the atomic level.

Besides imaging mode, the next most useful mode is diffraction mode, also called selected area diffraction, SAD, where the crystal lattice of a material is used as an interference pattern between the transmitted and diffracted beams, allowing the direct observation of the crystalline structure, as well as defects such as planar and line defects, grain boundaries, interfaces, etc., with atomic scale resolution. The brightfield/darkfield imaging modes of the microscope, which operate at intermediate magnification, combined with electron diffraction, are also invaluable for giving information about the morphology, crystal phases, and defects in a material. Another mode of the TEM is called microdiffraction, where the incident electron beam is focused (2 nm) to obtain the diffraction patterns from very small particles, allowing the identification of crystalline nanoparticles.

Figure 4.9 shows an example of the information that can be obtained from a HRTEM analysis. In that figure, a zinc sulfide (ZnS) thin film (<100 nm) deposited by spray pyrolysis was scratched from the substrate, and the particles were analyzed using a JEOL JEM2010 TEM working at 200 kV. The TEM image shows the morphology of the particles that resemble a rodlike structure. Moreover, the HRTEM images can be used to determine the interplanar distance of the crystalline structure (right corner), and, finally, the crystalline planes are further identified in the SAED pattern allowing the identification of the hexagonal ZnS structure using the ICDD diffraction database.

The addition of analytical methods, such as EDX or EELS, to obtain the composition of the samples at the microscale is also a great advantage. The main disadvantage of the TEM is the sample preparation process, since, as mentioned above, the sample must be thin enough to allow the transmission of the electrons with a minimum of inelastic scattering; ion beam erosion methods are usually required previous to the TEM analysis. For nanoparticles (NPs), the process is easier, and just a good distribution of dried NPs needs to be dispersed on appropriate microscopy grids.

4.2.2 Surface Topography

Surface topography or morphology can be observed by contacting or non-contacting techniques. The most commonly used contacting techniques are atomic force microscopy (AFM) and profilometry, while the most common non-contacting technique is optical or scanning electron microscopy.

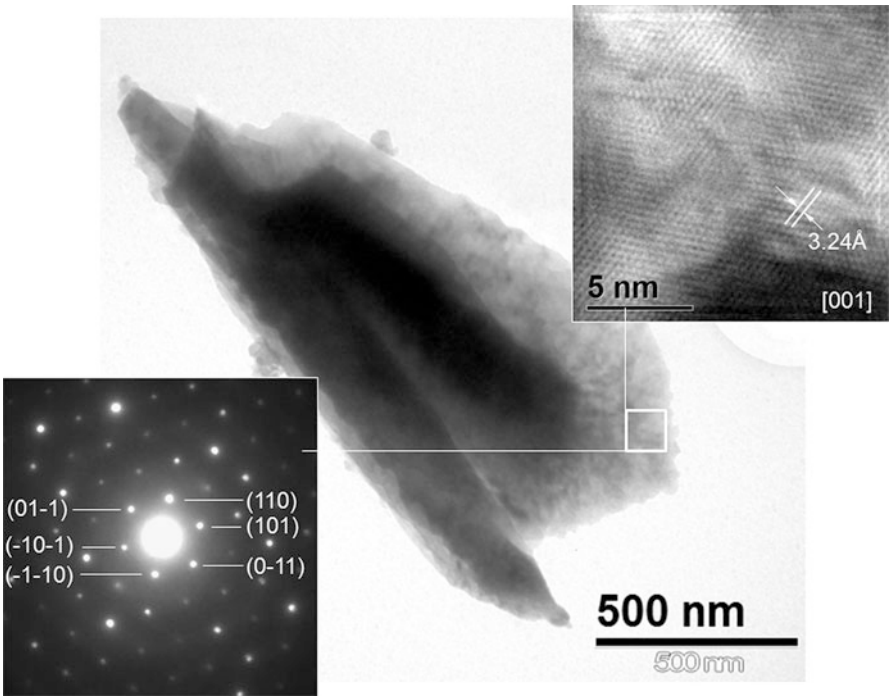

Fig. 4.9 TEM image of a particle obtained from a ZnS thin film. The HRTEM from the selected area and the microdiffraction pattern are also shown. Image provided by J. Santoyo, CINVESTAV, Mexico

4.2.2.1 Contact Techniques

Atomic force microscopy, AFM, is classified as a contact technique, although in some operation modes, no real contact occurs (Haugstad 2012; Eaton and West 2010; Moria et al. 2002). In the AFM, the probe consists of a sharp tip with radius of curvature of a few nanometers, normally made of Si or SiN, which is attached to a very sensitive cantilever. The tip is brought into close proximity to the surface of the sample, where the force between the tip and the sample leads to a deflection of the cantilever. The cantilever deflections are then measured with the aid of a laser and transformed into an analogous signal. The tip height (s) is regulated using a feedback mechanism and a piezoelectric piece above the tip, which allows the scanning of the sample without collisions. The tip height is plotted as a function of the sample dimensions (x, y) forming a topographic 3D image. The vertical resolution of the AFM is at the atomic level, about 0.1 nm, while the lateral resolution is about 1 nm. The area of the scans can be controlled from a molecular or atomic scale to about 100 μm^2, depending on the equipment. Other AFM modes measure different sample–tip interactions such as electrical (STM and Kelvin Probe), magnetic (MFM), piezoelectric (PFM), etc.

Profilometry is a real contacting technique where a stylus, to which a slight pressure is applied, is scanned across the surface. Profiles are formed by scanning the stylus along a direction keeping the stylus in contact with the surface at all moments; the displacements of the stylus in the vertical direction are measured and recorded. The stylus motion in the vertical direction is detected by piezoelectric or capacitors and is a direct measurement of the surface topography. The vertical resolution of the profilometry is lower (2 or 3 nm) than that of the AFM, but it can be used to obtain the surface roughness above the microscale, where AFM does not work.

Since both AFM and profilometry are sensitive to the vertical scale, surface topography can be quantified in terms of the surface roughness. Different definitions have been used to characterize the surface roughness; some of the most common are (1) the average roughness, R_a or S_a which are the arithmetic mean deviation of a lineal or a profile scan, respectively; (2) the RMS roughness, R_q or S_q which are the root mean square deviation of a lineal or a profile scan, respectively; and (3) the R_z or S_z and the R_t or S_t, which are a measure of maximum peak to valley distances in the lineal or profile scans.

4.2.2.2 Non-contact Techniques

Scanning electron microscopy (SEM) is a non-contacting technique where a beam of electrons, typically in the energy region of 0.2–40 keV, is focused on the sample's surface to form a spot of about 0.4–5 nm, which is scanned forming a 2D image of the sample (Goldstein et al. 2003; Goodhew et al. 2000; Amelinckx et al. 2008). The image can be formed by the secondary electrons (SEI), emitted from the valence and conduction bands of the material and whose intensity is proportional to the surface topography. The contrast difference produced from the emitted electrons at different heights (penetration field) produces a three-dimensional appearance in the image. However, images can also be formed by elastically scattered electrons (backscattered electrons, BSEI), and in such case the image contains information about the composition of the sample, since the contrast is due to electron–atom interaction, and so it is sensitive to the atomic mass. In modern microscopes, a composed SEI–BSEI image can be produced which contains both topography and composition information. The lateral resolution of the SEM can be as good as 1 nm when working at the highest incident electron energies; however, care has to be taken since the energy of the incident electron beam may damage the surface. The images obtained in the SEM are similar to the standard optical microscopes with a larger depth focus, which gives the impression of a 3D image. However, under normal operation condition, no quantitative information is obtained about the vertical scale.

For nanomaterials, high-resolution TEM (HRTEM) has also shown to be essential for studying the topography of the samples since high magnifications are required to really observe the detailed features, which might have a strong impact on the photocatalytic properties.

Finally, other methods to obtain information about the surface topography are the confocal optical microscopes and optical profilometers. However, they are not described here since they have not been extensively used for the photocatalytic samples.

4.2.3 Examples

Sridharan et al. (2013) reported the synthesis and visible light photocatalytic activity of graphitic C_3N_4–TiO_2 composites. In their synthesis, they obtained, in a first stage, microspheres of C- and N-codoped TiO_2 with stacked nanorods observed by SEM; however, the XRD pattern showed only the presence of pure tetragonal rutile phase of TiO_2. After pyrolysis in air at 300 and 500 °C, the XRD pattern corresponded again to pure rutile phase; however, XRD results alone were not conclusive since the diffraction peak formed at $2\theta = 27.4°$ matches both the (110) plane of rutile and the (002) plane of g-C_3N_4. Then, they used TEM to reveal the presence of two dimensional carbon nitride sheets with TiO_2 nanoparticles intercalated in between them, forming a TiCN composite, in the sample annealed at 300 °C. The spot diffraction pattern of the nanoparticle and its corresponding lattice resolved HRTEM image confirmed the single crystalline nature of the particles, while EDX spectra showed the presence of C, N, Ti, and O. The thermal treatment at 500 °C suppressed the formation of g-C_3N_4. The g-C_3N_4–TiO_2 composite showed an enhanced visible photocatalytic activity, attributed to the synergistic heterojunction formed between g-C_3N_4 nanosheets and doped TiO_2, that enhanced the electron–hole separation and the ability to absorb visible light.

Another interesting case of analysis is the one reported by Deng et al. (2012), who produced nanoporous ZnO microrods decorated with Ag nanoparticles. The XRD patterns showed the typical hexagonal wurtzite structure of ZnO. Additional peaks corresponding to the FCC Ag were identified, which increase their intensity as the Ag content increases. In addition, SEM images showed that the bare ZnO sample had rod shapes composed of nanoparticles. The microrods were about 90–150 nm in diameter and had a length of 0.5–3 μm. After the decoration with the Ag-NPs, the morphology looked the same, but further structural characterization with TEM showed that the sample had a typical nanoporous rodlike structure, and the 20–50 nm Ag-NPs were found attached onto the surfaces of the ZnO microrods (Fig. 4.10). HRTEM images revealed the interplanar spacing of about 0.28 nm, corresponding to the (100) plane of ZnO, while the interplanar spacing of 0.235 nm could be assigned to the (101) plane of Ag. Further composition analysis using XPS confirmed the presence of only Zn, O, Ag, and C, where the splitting of the 3d Ag peak indicated the metallic nature of silver, in agreement to other reported works (Lai et al. 2010; Lin et al. 2009). Additionally, they used Raman spectroscopy (RS) to evaluate the crystalline quality and the amount of defects as RS is sensitive to crystallization, structural disorder, and defects in micro- and nanostructures. The Raman spectra showed the Raman active modes for the hexagonal ZnO (A_1, E_1 and

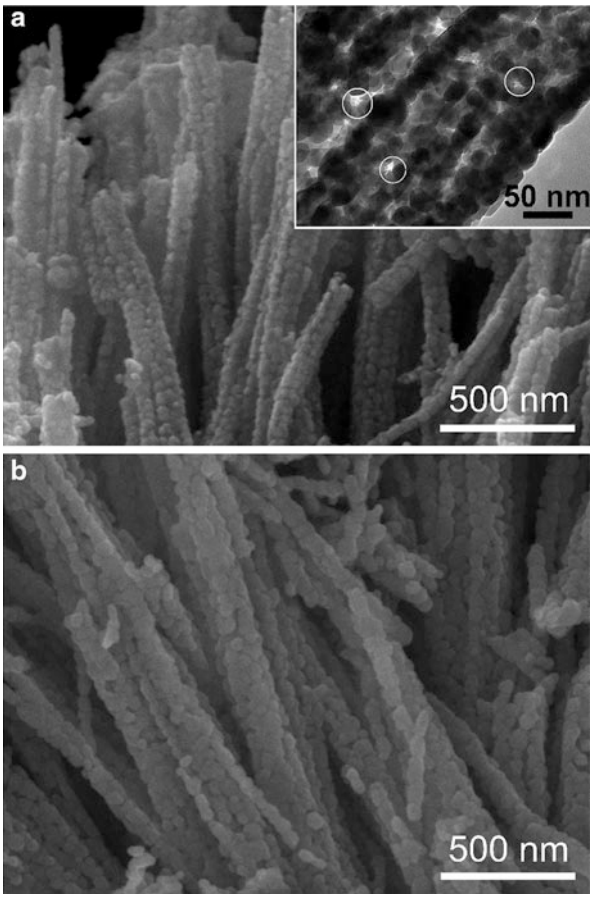

Fig. 4.10 (**a**) SEM image of the as-prepared n-ZnO microrods. The *inset* shows the high magnification view of TEM and (**b**) ZnO–Ag sample. From Deng et al. 2012. Copyright 2012 American Chemical Society

$2E_2$); the E_1 (longitudinal optical) mode, associated with the formation of oxygen deficiency, interstitial Zn, or the free charge carrier, was barely observed. Therefore, the appearance of a high intensity and dominated E_2 mode and almost no E_1 mode in the Raman spectrum indicated high quality crystalline specimens with little structural defects. The Ag-decorated ZnO microrods had a significant increase in the photocatalytic activity under solar light irradiation compared to the bare ZnO microrods, and the photostability was highly improved. This was attributed to the unique nano-/micro-configured structure achieved and to the Ag-NPs that acted as electron wells promoting the charge separation.

The effect of the topography on the wettability, the antifogging properties, and the photocatalytic activity of SiO_2–TiO_2 nanoparticle coatings was studied by Li and He (2013). The SEM and AFM images showed that hierarchically raspberry-like structures were produced showing superhydrophilic, antifogging, and photocatalytic activity toward organic pollutants, being the surface nanotopography the main responsible for the properties.

Graphene and graphene oxide have demonstrated to have extraordinary properties with potential applications in many fields, including photocatalysis. It is particularly attractive for the photo-induced water reduction to produce H_2, the fuel of the future. During the synthesis and functionalization of graphene sheets, AFM and optical microscopy are crucial characterization techniques as shown by Zhu et al. (2013) and Liu et al. (2013b), which used AFM to measure the number of graphene layers or the functionalization of the graphene.

As a final example of the effect of structure and topography in the photocatalytic properties, the ZnO–carbon nanotube (CNT) nanocomposites produced via a simple sol method are presented (Ahmad et al. 2013). The composites were produced at different concentrations of ZnO (0–20 wt %), and the photo-, sono-, and sonophotocatalytic degradation of the rhodamine blue was investigated, finding that the response was always higher for the combined process but was dependent on the ZnO concentration. In order to understand the role played by the CNTs, a wide range of characterization techniques were used. The SEM, TEM, and HRTEM showed the morphology and distribution of the ZnO nanoparticles attached to the multi-walled carbon nanotubes. Meanwhile, other techniques, such as BET, XPS, photoluminescence (PL), and DRS measurements, demonstrated that all the ZnO/CNT nanocomposites have stronger light absorption in the visible light region compared to pure ZnO, effect that acted synergistically with a larger specific surface area of the composites and the fact that the CNTs act as electron acceptors for ZnO, hindering the recombination of charge carriers.

4.3 Surface Area and Porosity

Surface area and porosity are important parameters for the photocatylic applications. The standard methods to determine these properties include direct observation by optical or electronic microscopy, gas adsorption, mercury porosimetry, as well as small angle scattering of X-rays (SAXS) or neutrons (SANS). Since the particle size for powders or nanopowder samples is directly related to the surface area, light scattering methods can also be used to determine indirectly the surface area.

4.3.1 Gas Adsorption

Gas adsorption methods are the most commonly used based on the adsorption of an inert gas, mainly nitrogen, on the surface of a solid material (Condon 2006; Lowell et al. 2004).

Gas adsorption occurs on the outer surface and, in case of porous materials, also on the surface of pores and allows the determination of the specific surface area (SSA). Several methods are used for SSA determination (i.e., Brunauer, Emmett,

and Teller (BET) and de Boer *t*-Plot methods); nevertheless the BET method is the most commonly used, and it provides precise specific surface area evaluation by nitrogen multilayer adsorption, measured as a function of relative pressure using a fully automated analyzer (Brunauer et al. 1938).

Monolayer formation of gas molecules on the surface is used to determine the specific surface area, while the principle of capillary condensation can be applied to assess the presence of pores, pore volume, and pore size distribution. The technique encompasses external area and pore area evaluations to determine the total specific surface area in $m^2\ g^{-1}$.

According to IUPAC (Sing 1985), an adsorption isotherm is the function which relates the amount of adsorbed adsorbate to the pressure (or concentration) of the adsorbate in the fluid phase under equilibrium condition. IUPAC also classified adsorption isotherms into six types as shown in Fig. 4.11. The detailed discussion of the shape of adsorption and desorption isotherms can be found in Sing (1985) and Lowell and Shields 1984.

As can be seen in Fig. 4.10, type IV and V exhibit a hysteresis loop, i.e., the adsorption and desorption isotherms do not coincide over a certain region of external pressures. The type IV isotherm is typical for mesoporous adsorbents. Type V hysteresis loop is a typical sign of a weak fluid–wall interaction. It is less common but observed with certain porous adsorbents. Measuring sorption scanning curves helps to identify the underlying mechanism of hysteresis, which is crucial for obtaining an accurate and comprehensive pore size analysis of mesoporous and micro-mesoporous materials.

Pore width, pore shape, and the effective adsorption potential are the factors that determine pore filling. In the case of so-called micropores (pore width <2 nm, according to IUPAC classification), pore filling occurs in a continuous way, whereas in case of mesopores (pore widths in the range from 2 to 50 nm) pore filling occurs by pore condensation, which reflects a first-order gas–liquid phase transition. So-called classical macroscopic, thermodynamic concepts are based on the assumption of a certain pore-filling mechanism. Methods based on the Kelvin equation (e.g., Barrett–Joyner–Halenda, the BJH method) are linked to the pore condensation phenomena, i.e., they are applicable for mesopore size analysis, but they fail to describe the pore filling of micropores and even narrow mesopores in a correct way. In contrast to these macroscopic approaches, methods like the density functional theory (DFT) or methods of molecular simulation (Monte Carlo simulation methods (MC), molecular dynamics methods (MD)) provide not only a microscopic model of adsorption but also a more realistic description of the thermodynamic properties of the pore fluid (Thommes Quantachrome). The pore shape can further be obtained from the hysteresis loop from corresponding isotherm.

A detailed description of isotherm types, hysteresis loop, and methods related with gas adsorption in porous materials mentioned above can be found in several articles and books already published (Sing 1985; Lowell and Shields 1984; Brunauer et al. 1938; Barrett et al. 1951; Fagerlund 1973; Gauden et al. 2004; Kowalczyk et al. 2003; Lastoskie and Gubbins 2000; Dombrowski et al. 2001; Rouquerol et al. 2014).

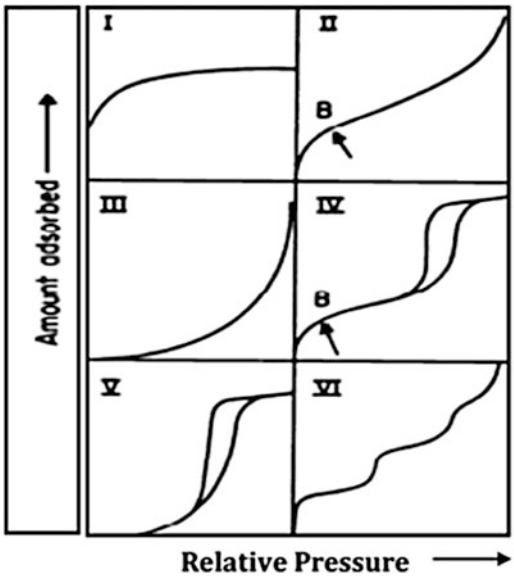

Fig. 4.11 Classification of adsorption isotherms (IUPAC, Sing 1985)

4.3.2 Mercury Porosimetry

Mercury porosimetry uses the non-wetting properties of mercury to gain information on the porosity, pore volume, pore size distribution, and density (Lowell et al. 2004). The technique consist of applying a high pressure (about 400 MPa for the smallest pores) to force the intrusion of mercury in the sample's small pores, whereas mercury intrusion in larger pores already occurs at low pressure. In this way a wide dynamic range of pore sizes can be measured, and the pore size distribution can be obtained starting from 4 nm up to approx. 800 μm. Thus, mercury porosimetry is extremely suitable for materials showing broad distributions of pore sizes or mainly macropores.

4.3.3 Dynamic Light Scattering

Light scattering techniques have become very popular these days to measure the size and size distribution of nanoparticles in a solution. Basically, the techniques consist of shining a monochromatic light beam, such as a laser, onto the solution that contains the spherical particles (Schartl 2007). The Brownian motion of the particles (movement of particles due to the random collision with the molecules of the liquid that surrounds the particle) causes a scattering of the light intensity, and such scattering depends on the particle velocity. For Brownian motion, small particles move quickly and large particles move more slowly. Therefore, the

measurements of the intensity of the light by a photomultiplier placed at 90° as a function of the frequency leads to a frequency spectrum of the intensity of the scattered light. The spectra will have the form of a Lorentzian shaped line whose width depends on the diffusion coefficient, D, and the scattering angle. The assumption of pure Brownian movement and spherical particles allows the determination of size and size distribution of particles and molecules. This is possible, since the probability density function for Brownian movement is well defined and depends mainly in the diffusion coefficient, which according to the Stokes–Einstein equation is a function of the temperature, the viscosity of the solvent, and the size of the particle.

4.3.4 Examples

Porous TiO_2-coated magnetic core-shell nanocomposites were prepared by Liu et al. (2013a) in order to improve the separation and recovery of nanosized TiO_2 while maintaining good catalytic activity. The nanocomposite was formed by magnetic Fe_3O_4 particles covered with an interlayer of SiO_2 and an outer layer of porous anatase TiO_2 ($TiO_2/SiO_2@Fe_3O_4$ microspheres). The XRD pattern presented the characteristic peaks of anatase TiO_2 and the peaks of cubic Fe_3O_4. The N_2 adsorption–desorption isotherms were acquired. The samples exhibited a combination of type I and IV patterns with distinct H2 and H4 hysteretic loops, which confirmed the existence of micro- and mesoporous in the outer layer of anatase. Such multiple-pore structure can promote rapid diffusion of various reactants and products during the photocatalytic reaction and enhance the photocatalytic activity. The BET surface area of the 9 %TiO_2/6 %$SiO_2@Fe_3O_4$ microspheres was 373.5 m^2g^{-1}, and the BJH pore volume was 0.28 cm^3g^{-1}. This material was 20 % more efficient than P25 in the degradation of methylene blue and methyl orange. The high photocatalytic performance was maintained after six cycles. The samples presented a high degree of superparamagnetism; although the magnetization values were weak compared to pure Fe_3O_4, they are strong enough to guarantee a good recovery by magnetic separation.

Recently, ZnO nanostructures have gained a lot of attention; particularly, nanorods are potentially useful in photocatalysis due to a high surface area. Hafez (2012) used a simple hydrothermal method to obtain ZnO rodlike nanostructures with pointed-shape ends. TEM images showed straight and uniform rodlike structures with diameters between 30 and 50 nm and length between 400 and 650 nm. XRD pattern indicated the hexagonal wurtzite structure of ZnO, while EDS analysis confirmed the presence of only Zn and O without any other elemental contamination (Fig. 4.12). The N_2 adsorption/desorption measurements showed a type II isotherm with small type H3 adsorption hysteresis loop. The BET surface area of the nanorods was about 270 m^2g^{-1}. The pore size distribution presents two types of pores (small mesopores at 1–5 nm and large meso- and macropores centered at 10–100 nm) (Fig. 4.13). Additionally the hysteresis loop approached $P/P_o = 1$,

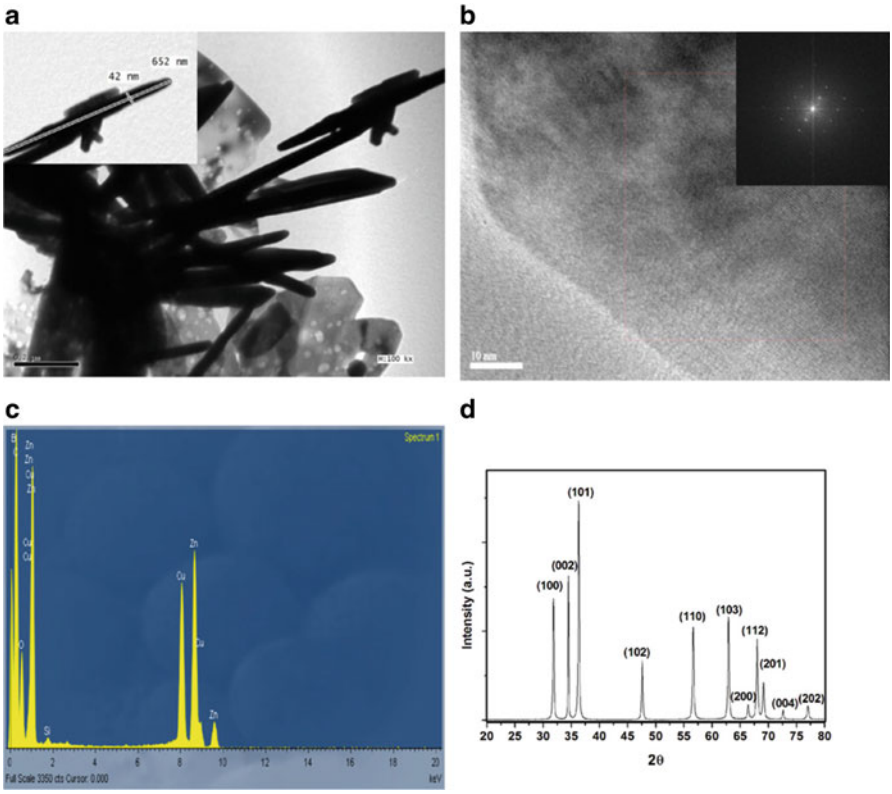

Fig. 4.12 (**a**) TEM image; (**b**) SAED; (**c**) EDX; (**d**) XRD patterns of the obtained ZnO rodlike nanostructures. From Hafez 2012

confirming the presence of macropores (>50 nm). In fact, the nanorod structures did not contain mesopores and macropores; the observed micro- and mesopores came from the aggregation of the nanorods which leads to formation of such porous structure and this high surface area. The sample exhibited good photocatalytic activity in the degradation of reactive yellow 15 dye that can be attributed to the high adsorption percentage (34.7 %) of the dye on the surface of the catalyst as a consequence of the high surface area.

4.4 Vibrational Spectroscopies

Vibrational spectroscopies are widely used techniques to characterize materials because they are nondestructive, noninvasive tools that provide information about the molecular composition and structure. These two analytical techniques, namely,

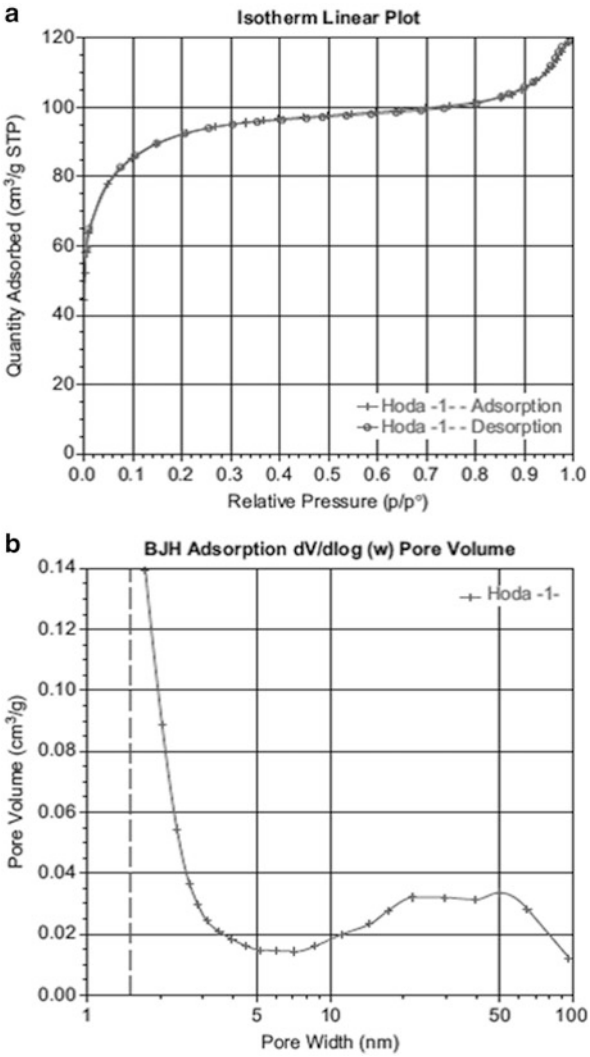

Fig. 4.13 (**a**) Nitrogen adsorption–desorption isotherm and (**b**) BJH pore size distribution of the ZnO rodlike nanomaterials. From Hafez 2012

infrared and Raman spectroscopy, measure vibrational energy levels which are associated with the chemical bonds in the sample. The spectrum is unique, like a fingerprint, and vibrational spectroscopy is used for identification, characterization, structure elucidation, reaction monitoring, and quality control. FTIR and Raman have been implemented for in situ characterization of catalytic reactions (Haw 2002).

4.4.1 Fourier Transform Infrared Spectroscopy, FTIR

Infrared spectroscopy is a technique based on the detection of the vibrations of the atoms of a molecule by measuring the absorption of electromagnetic light by the sample (Kuzmany 2010). An infrared spectrum is commonly obtained by passing infrared radiation through a sample (transmission) and determining the particular energy at which light is absorbed. The IR energy range (700 nm to 1 mm or 1.24 meV to 1.7 eV) coincides with the energies needed to excite fundamental modes of rotation and vibration in materials; thus absorption of the incident IR signal is due to the excitation between ground and excited vibrational states. The transmission or reflection (attenuated total reflectance (ATR) mode or diffuse reflectance) spectra show the specific vibrational modes, characteristic of each molecular structure that depends on the bond strength, structure, masses of the atoms, etc. IR spectroscopy is a nondestructive technique which can be used in any type of samples: gases, liquids, solids, powders, fibers, etc. It is very surface sensitive and can detect very small quantities of molecules such as 10^{-5} monolayers. Infrared light interacts only with those vibrations whose dipole moment (μ) periodically changes due to the oscillation of the atoms. If the oscillating electromagnetic field of the incident photon couples with the dipole oscillating at the same frequency, it is absorbed. Those vibrations that are not accompanied by a change in the dipole moment are IR-inactive, but may be Raman active if the polarizability (α) of the electron configuration changes in the course of an oscillation period.

4.4.2 Raman Spectroscopy

Raman spectroscopy provides information about molecular vibrations that can be used for sample chemical identification and quantitation. In Raman spectroscopy, the sample is excited by a monochromatic light source (i.e., laser in the visible, near-IR, or near-UV range, 1–12.4 eV), and the scattered light is detected (Ferraro et al. 2003). The majority of the scattered light is of the same frequency as the excitation source (Rayleigh or elastic scattering). A small fraction of the scattered light (ca. 5–10 % of the incident light intensity) is shifted in energy from the laser frequency due to interactions between the incident electromagnetic waves and the vibrational energy levels of the molecules in the sample. Plotting the intensity of the Raman shift (scattered minus Rayleigh energy) versus frequency results in a Raman spectrum of the sample, where the peak positions will lie at frequencies that correspond to the energy levels of different functional group vibrations, and the spectra can be analyzed similar to IR. The energy shift of the scattered photons is independent of the energy of the incident photons, except for resonance phenomena, and is characteristic of the chemical bonds, electronic configuration, and vibrational modes that were excited. In the same sense as in IR spectroscopy, it is possible to characterize the surface chemistry from the generated spectrum which is

a fingerprint of the molecular structure. Although the physical process and instrumentation of Raman spectroscopy is more complex, it has the advantage of being more versatile due to the different incident energies; it is nondestructive and less affected by the environment. Moreover, the new Raman systems are highly sensitive, and chemical imaging has also been developed, as well as in situ analysis of surface processes (Lamberti et al. 2010).

4.4.3 Examples

FTIR technique can be very useful for the identification of chemical bonds present in the sample and thus confirm a specific structure, especially for complex compounds. Such is the case of photocatalytic graphitic carbon nitride compounds (Yan et al. 2009; Huang et al. 2013; Dante et al. 2013), which presents strong bands in the 1,200–1,650 cm^{-1} region that correspond to the typical stretching modes of CN heterocycles. Additionally, the characteristic breathing mode of the triazine units at 801 cm^{-1} is observed. The presence of a broad band at around 3,000–3,500 cm^{-1} is indicative of NH stretching vibration modes. In polymeric carbon nitride obtained from melamine cyanurate, this band can evolve toward a definition of four bands when the pyrolysis temperature is increased from 450 to 700 °C (Dante et al. 2013); the bands appearing at 3,248, 3,150, and 3,078 cm^{-1} are due to NH interacting via hydrogen bond, as observed in Fig. 4.14. FTIR spectra at 650 and 700 °C

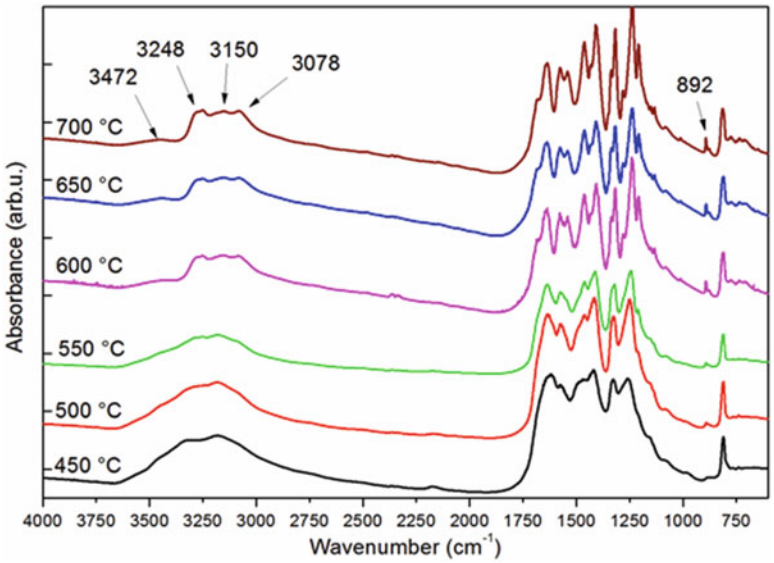

Fig. 4.14 FTIR spectra of polymeric carbon nitride obtained from melamine cyanurate at 650 and 700°

correspond substantially to a melon (polymeric carbon nitride) which is known to consist of heptazine units, observed at 892 cm^{-1} that increase with the temperature (Horvath-Bordon et al. 2004).

Liang et al. (2012) hybridized Ag_3PO_4 nanospheres with graphene oxide (GO) sheets and used FTIR and Raman spectroscopy to demonstrate the existence of strong charge interactions. They obtained the FTIR spectra of pure GO and pure Ag_3PO_4 and compared them with the spectrum of the GO–Ag_3PO_4 nanocomposite. The latter showed a shift in the peak associated with the carbonyl group due to charge interactions with the Ag_3PO_4 nanospheres. The characteristic peak assigned to the stretching vibration of the P–O–P group also shifted to a higher wavenumber, suggesting that Ag_3PO_4 successfully attached with GO sheets. Moreover, Raman spectroscopy, an important tool for investigating the detailed structure of graphitic materials, was applied to roughly evaluate the disorder degree in the hexagonal graphitic layers and the average size of the sp^2 domains of the graphite materials. They obtained the intensity ratio of the D and G bands for the GO sheets and the GO–Ag_3PO_4 nanocomposite, finding an increase in this ratio from 1.13 of GO to 1.21 of the composite, indicating a larger amount of defects formed in the graphitic layers after the incorporation of the Ag_3PO_4 nanospheres. The interactions are not only beneficial to improve the stability but also favorable to enhance the photocatalytic activity of Ag_3PO_4. In an interesting experiment, reflection absorption infrared spectroscopy (RAIRS) was used to compare the photocatalytic activity of TiO_2 polymorphs (Mingchun Xu et al. 2011); the anatase (101) surface was more active for the photo-oxidation of CO into CO_2 than the rutile (110). The authors explained the difference as a consequence of a one order of magnitude larger electron–hole lifetime for the anatase surface than rutile, information obtained from transient photoconductance experiments. This is a key experiment providing evidence to support the commonly observed different photocatalytic activities for the two polymorphs.

Raman spectroscopy, on the other hand, has been more used for either phase identification, temperature-induced phase transformation, determination of quality of the synthesized material, or detection of carbonaceous residues left during the synthesis (Hardcastle 2011; Beuvier et al. 2009). However, care has to be taken when analyzing nanocrystalline materials since it has been shown that Raman shift position and line width change in comparison to bulk materials. The changes in the Raman spectra of nanocrystalline TiO_2 have been interpreted as due to phonon confinement, non-stoichiometry, or internal stress (Balaji et al. 2006; Swamy et al. 2005 and references therein).

4.5 Optical Properties

Semiconductors and insulators have the fundamental band gap in the near infrared, visible, or ultraviolet spectral region (Fox 2010). Therefore, light absorption is zero below the absorption edge, and it increases rapidly once the energy of the light is

enough to excite electrons across the optical gap, which is called interband transition and is related to the band structure of the material. The physical model for such process is based on the application of the quantum mechanical description of the light–matter interaction to the band states of solids. The optical interband transitions occur when a photon excites an electron from the filled valence band to the empty conduction band. The threshold for absorption occurs when the photon energy equals the band gap energy (E_g), and after there is a continuous absorption spectrum up to an energy which depends on the specific structure of the bands involved. The band structure also determines the interband absorption rate, since it depends on the population of the bands (density of states), as well as in other quantum-mechanically (QM) defined selection rules. The interband absorption creates a hole in the valence band and puts an electron in the conduction band, which is typically referred as the creation of an electron–hole pair. The frequency or energy dependence of the absorption coefficient, $\alpha(\omega)$, contains all the information concerning the light–matter interaction and therefore is QM determined by the probability of exciting an electron from an initial to a final quantum state by the absorption of a photon. This calculation leads to the following simplified equations: for any semiconductor,

$$\text{For } \hbar\omega < E_g, \quad \alpha = 0 \tag{4.5}$$

However, as the photon energy increases, for a direct gap semiconductor, as in Figure 4.15(a)

$$\text{For } \hbar\omega \geq E_g, \quad \alpha \propto \left(\hbar\omega - E_g\right)^{1/2} \tag{4.6}$$

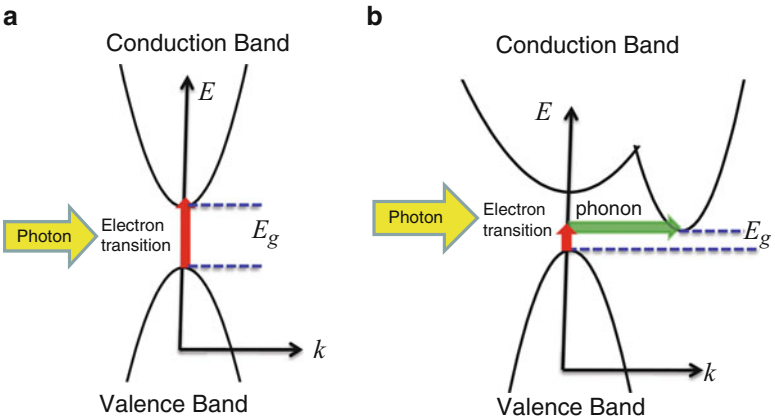

Fig. 4.15 Interband transition in solids. (**a**) Direct gap and (**b**) indirect gap. Since the phonon energies are much lower than the optical gap, it is very common to neglect it for an estimation of the gap

For an indirect gap semiconductor, as in Figure 4.15(b)

$$\text{For } \hbar\omega \geq E_g, \quad \alpha \propto \left(\hbar\omega - E_g \mp \hbar\Omega\right)^2 \tag{4.7}$$

where $\hbar\Omega$ is the phonon energy that assists the transition process, as shown in Fig. 4.15. Some authors used $\alpha\hbar\omega \sim (\hbar\omega - E_g)^p$ where the exponent is the same as before and the energy factor introduces only a small correction to the gap values.

Optical gap calculations for solids are usually done using one of the equations in Eq. (4.6) or (4.7). For this, the absorption coefficient has to be obtained experimentally by some of the methods described later, and the optical gap can be calculated by plotting

$$\alpha^2 \text{ vs. } \hbar\omega \text{ for a direct gap} \tag{4.8}$$

$$\alpha^{1/2} \text{ vs. } \hbar\omega \text{ for indirect gap} \tag{4.9}$$

From such plots, the E_g is calculated as the point at which a linear extrapolation of the relations (Eqs. 4.8 and 4.9) crosses the energy axis at $\alpha = 0$, as illustrated in Fig. 4.16.

The study of amorphous semiconductors brought a lot of attention during the 1960s, for the development of amorphous silicon and germanium and their possible applications in the newly born microelectronic industry (Tauc et al. 1966; Cody et al. 1982). Such studies proposed certain models to estimate the optical band gap for the amorphous semiconductors considering that the optical transitions conserve energy but not the momentum vector and that the densities of states near the band extreme have the same energy dependence as in the crystalline counterparts. The most known of such models is the Tauc-gap model (Tauc et al. 1966) which states that the absorption edge follows Eq. (4.10):

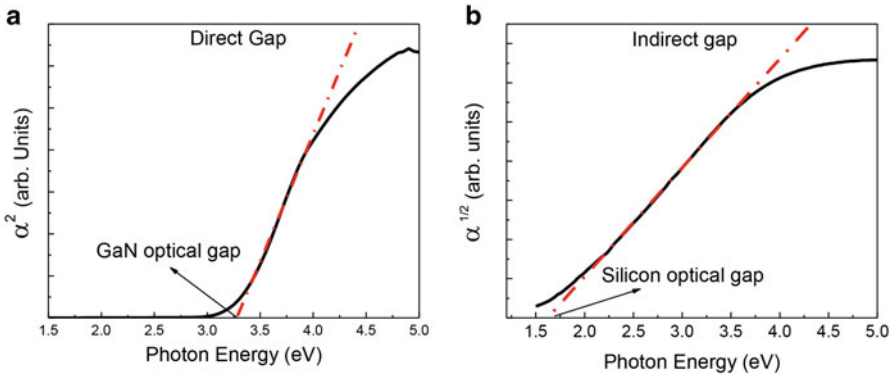

Fig. 4.16 Example of the calculation of the optical gap for standard semiconductors. (**a**) GaN direct gap and (**b**) Si indirect gap

$$\omega^2 \epsilon_2 \sim (\hbar\omega - E_g)^2 \tag{4.10}$$

where ϵ_2 is the complex dielectric function, related to the refractive index and the extinction coefficient as $\epsilon_2 = 2nk$. Using Eq. (4.11) that relates the absorption coefficient with the extinction coefficient,

$$\alpha(\lambda) = \frac{4\pi k(\lambda)}{\lambda} \tag{4.11}$$

where λ is the light wavelength, the Tauc-plot equation is given by

$$\sqrt{\alpha(\hbar\omega)} \sim (\hbar\omega - E_g) \tag{4.12}$$

And so the optical gap for amorphous semiconductors is estimated plotting $\sqrt{\alpha(\hbar\omega)}$ versus $\hbar\omega$, which is similar to Eqs. (4.8) and (4.9), but care has to be taken since for amorphous semiconductors the direct–indirect concept is no longer valid.

4.5.1 Transmission and Reflection

For low absorbing materials, the absorption coefficient can be calculated from the equation

$$T = (1 - R)^2 \exp(-\alpha d) \tag{4.13}$$

where T is the transmission, R is the reflectance, and d is the sample thickness (Fox 2010).

T and R are measured as the fraction of light intensity transmitted or reflected from an optical medium in comparison to the intensity of an incident light. The spectral dependence of T and R are measured with the aid of a monochromator.

As Eq. (4.13) shows, it is important to measure both T and R, although in many cases R is neglected and so the absorption coefficient is estimated only from the T spectra. However, it is important to understand that such model gives only approximate absorption coefficients, since reflection from semiconductor samples in the UV–Vis region can be as high as 30 %, as shown in Fig. 4.17 for different materials.

Another method to analyze the T and R spectra (particularly useful when the absorption is larger) which is valid for homogeneous materials and smooth surfaces, in which scattering losses are negligible, is to use the total transmission and reflection coefficients for normal incidence (Fresnel coefficients) and calculate the dispersion of both the refractive index (n) and the extinction coefficient (k). In this case, the absorption is calculated from Eq. (4.11).

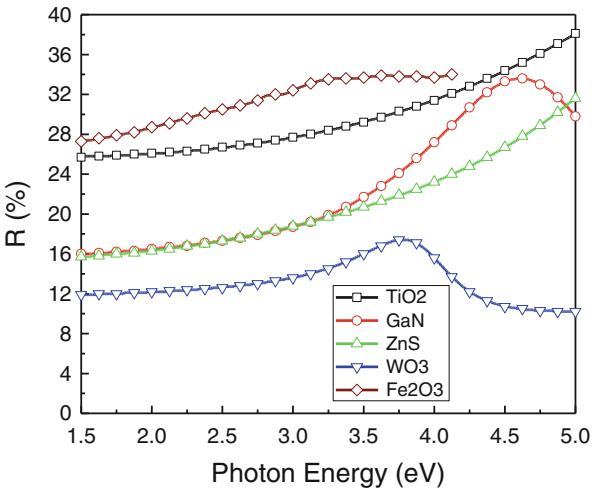

Fig. 4.17 Reflectance spectra of different semiconductor slabs estimated using their known optical properties (n, k)

Some specific software uses minimization algorithms to solve iteratively the system of equations (Eqs. 4.14 and 4.15), where the film thickness could be also a fitting parameter:

$$T_{\text{cal}}(n,k,\lambda) - T_{\text{exp}}(\lambda) = 0 \tag{4.14}$$

$$R_{\text{cal}}(n,k,\lambda) - R_{\text{exp}}(\lambda) = 0 \tag{4.15}$$

Multiple solutions are a usual problem in this type of calculation; however when R and T are measured under the same conditions, the multiple solutions for k do not deviate considerably from the true values, so that the problem is mainly restricted to the refractive index, a problem that can be reduced having previous knowledge of the film thickness.

4.5.2 Diffuse Reflectance

For the case of nonhomogeneous, opaque, or powdered materials, the determination of the band gap is not possible using either the optical transmission–reflection or the spectroscopic ellipsometric methods. Measurement of the diffuse reflectance instead is a more adequate technique (Murphy 2007a). Diffuse reflectance spectroscopy (DRS) is a suitable technique to measure optical properties of rough surfaces or powders. This technique also provides information about the oxidation state and coordination environment of transition metal ions in catalytic solids. If the surface of the material or sample is microscopically rough, the light rays will reflect and diffuse in many different directions. In this case, each individual ray follows the law of reflection. However, the roughness of the material makes that each

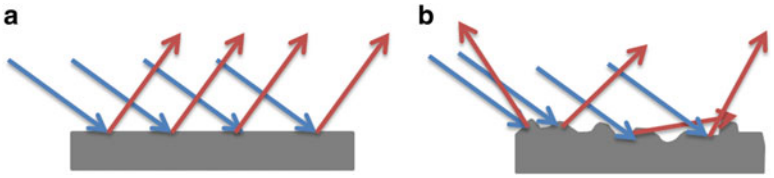

Fig. 4.18 Comparison between (**a**) specular reflectance (smooth surfaces) and (**b**) diffuse reflectance (rough surfaces)

individual ray meets a surface with different orientation. Subsequently, when the individual rays reflect off the rough surface, they scatter in different directions (see Fig. 4.18).

When electromagnetic radiation is incident upon a system which is able to scatter as well as absorb photons, Lambert–Beer's law is no longer useful due to two main reasons; first, the path length l is no longer well defined, and, second, the optical response is no longer determined by k but by $\hat{n} = n - ik$ (Delgass et al. 1979).

The diffuse reflectance phenomenon is complex, but in the simplest case of a nonabsorbing material ($k = 0$), it involves only scattering of photons. The scattering of light can be divided into three different regimes: (1) single scattering, (2) multiple scattering, and (3) dependent scattering (Weckhuysen et al. 2000). The first type arises when scattering centers are sufficiently apart that each is illuminated only by photons not previously scattered, and on average, there is no phase relationship between the photons scattered form the neighboring particles. In the case of multiple scattering, the scattering centers are still far apart that they may be treated as independent, but each center is now illuminated by photons scattered from adjacent particles. Dependent scattering arises when, in addition to multiple scattering, phase coherence exists between scattered photons from adjacent centers. Dependent scattering is present if the average distance (d) between scattering centers is less than three times the particle diameter.

The division of light scattering systems into the above three categories determines the theoretical approach necessary to describe the scattered light intensity. For single and multiple scattering, the absence of phase coherence ensures that the total scattered light intensity is merely the sum of the intensities of the individual scatters. Both types of scattering can be mathematically treated in a rather easy way. In contrast, when the particles become so tightly packed that phase coherence becomes important, amplitudes rather than intensities must be summed. This is the case for heterogeneous catalysts because they are always investigated in the form of densely packed powders. Then the radiation transfer theory has to be considered, leading to the well-known Kubelka–Munk theory. The Kubelka–Munk model uses an effective scattering coefficient S and an effective absorption coefficient K to describe the optical properties of a compact powder sample; a sufficiently thick sample so that all the incident light is absorbed or scattered, no light is considered.

Then, the Kubelka–Munk (K-M) function, $F(R_\infty)$, is related to the apparent absorption (K) and the apparent scattering coefficient (S) by Eq. (4.16):

$$F(R_\infty) = \frac{(1 - R_\infty)^2}{2R_\infty} = \frac{K}{S} \tag{4.16}$$

Where $\left(R_\infty = \frac{R_{\text{sample}}}{R_{\text{standard}}}\right)$, and it is the equivalent of the Lambert–Beer law for dilute species measured by diffuse reflectance experiments:

$$F(R_\infty) = \frac{\varepsilon C}{s} \tag{4.17}$$

Where ε is the molar absorptivity and C the concentration.

For such powder infinitely thick samples, the optical band gap can be easily calculated using Eqs. (4.8) and (4.9) but substituting α by $F(R_\infty)$

However, as discussed by Murphy (2007a), when a thin powder sample (<1 mm) or a rough thin coating on a substrate is measured using DRS, the reflection and transmission of the light through the different interfaces need to be taken into account to avoid the thickness dependence of the optical gap. For this, Murphy (2006, 2007b) proposed a modified K-M two-flux model to calculate the reflectance of the coating as a function of the refractive index, absorption coefficient, scattering coefficient, and thickness. Then a fitting procedure is used to correlate the calculated reflectance spectra to the measurements using a spectral projected gradient algorithm, and in this way, appropriate optical properties can be obtained.

DRS measurements are achieved using a UV–Vis (can also be used for infrared analysis) spectrophotometer, but with a special accessory called integrating sphere. This accessory provides the ability to collect a quantitative reflectance spectrum from highly scattering or irregularly shaped samples, but acquiring only diffuse light, not the specular signal and so the K-M theory can be applied.

4.5.3 Spectroscopic Ellipsometry

Optical ellipsometry is a common method used to determine dielectric functions or complex refractive index, thickness, and morphology of thin films of various natures, but requires flat surfaces. Ellipsometry measures the change of the light polarization upon reflection at an interface (Tompkins and Irene 2005; Fujiwara 2007). In ellipsometry, the amplitude ratio and the phase difference between the parallel (p) and the perpendicular (s) components of the reflected light polarized with respect to the plane of incidence are measured and expressed by two quantities, namely, the ellipsometric angles, psi Ψ (which measures the amplitude ratio) and delta Δ (which measures the relative phase change). These are given by

$$\overline{\rho} = \frac{\overline{r}_p}{\overline{r}_s} = \frac{|r_p|\exp(\delta_p)}{|r_s|\exp(\delta_s)} = \frac{|r_p|}{|r_s|}\exp(\delta_p - \delta_s) = \tan(\Psi)\exp(i\Delta) \tag{4.18}$$

where the tilde in r_p and r_s represents that they are the complex reflections coefficients for the p and s components of the electric field, respectively. For bulk samples, r_p and r_s are the Fresnel coefficients, and for thin films on a substrate, r_p and r_s are substituted by the total reflection coefficients R_p and R_s given by

$$\overline{R}_{p,s} = \frac{E^R_{p,s}}{E^0_{p,s}} = \frac{\overline{r}_{0,1p,s} + \overline{r}_{1,2p,s}e^{i2\beta}}{1 + \overline{r}_{0,1p,s}\overline{r}_{1,2p,s}e^{i2\beta}} \text{ and} \tag{4.19}$$

$$\beta = 2\pi\left(\frac{d}{\lambda}\right)\sqrt{\overline{n}_1^2 - n_0^2\sin^2\theta} \tag{4.20}$$

where $\overline{r}_{0,1p,s}$ and $\overline{r}_{1,2p,s}$ are the Fresnel coefficients for the interfaces between media 0 and 1 and between media 1 and 2, respectively, d is the film thickness, λ is the wavelength, and θ the incidence angle, as shown in Fig. 4.19.

The advantage of ellipsometry over conventionally transmission–reflection measurements is that ellipsometry measures the ratio between two quantities, so it is potentially more precise and accurate. However, the disadvantage is the complexity of the optical system.

In the most general case the reflecting surface is made up of a stack of planar multilayer materials, and then polarization change, ρ, depends on the incidence angle, the radiation wavelength, and the thickness and complex refraction index of each layer. The thickness and complex refractive index of the layers are obtained from measurements of $\Delta(\lambda)$ and $\Psi(\lambda)$ by fitting the experimental data with a suitable optical model of the system under consideration.

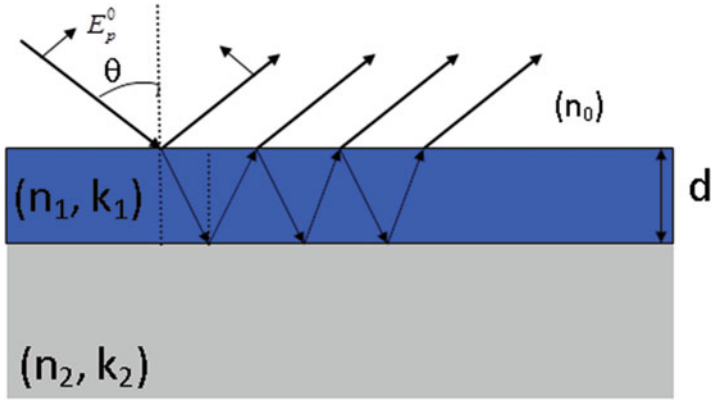

Fig. 4.19 The light pathway for a transparent film on an absorbing thick substrate

The development of digital light detectors together with the need for faster acquisition, having the capability of measuring psi and delta even if the sample was continuing changing (to study film growth), led to the development of various approaches for the determination of the polarization state of transverse electromagnetic plane waves, such as the rotating analyzer ellipsometer, the rotating polarizer ellipsometer, and the phase modulation ellipsometer. These dynamic measurements are based on the idea that one of the parameters that describes the optical component of the system is periodically varied with time and the detected signal is Fourier-analyzed. The different hardware configurations together with their advantages and disadvantages have been extensively discussed in many papers.

Ellipsometry does not directly measure the film thickness or optical constants; it measures psi and delta. To extract useful information about the sample, it is necessary to perform a model-dependent analysis of the ellipsometric data. Therefore, after the measurements are made, a model for the optical structure of the sample is constructed. This may include a substrate and a single film on top, or substrate plus film with roughness on top, or more complex multilayered structures. Assuming a sample structure and dispersion formulae for the optical constants of the different layers, the measured ellipsometric spectra are then fitted using a standard minimization algorithm; an example of the fitting for a Bi_2O_3 thin film deposited on a silicon substrate by magnetron sputtering is shown in Fig. 4.20.

The optical constants of the layers are simulated using dispersion formulae (Fujiwara 2007; Tompkins and Irene 2005) such as the following:

- The Classical Lorentz oscillator model, which allows a fairly good visualization of the atom–field interactions, considers the material medium as an assemblage

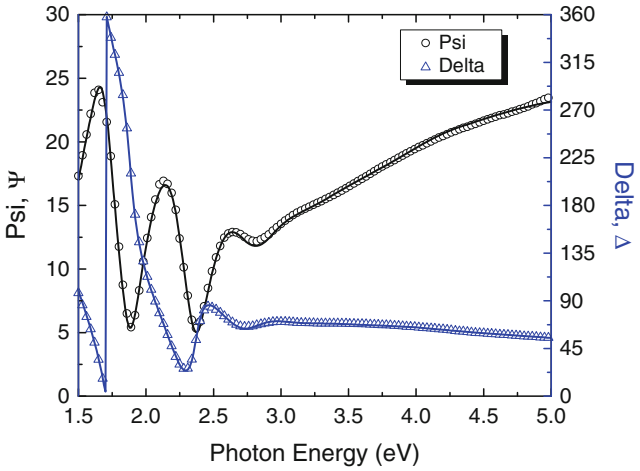

Fig. 4.20 Ellipsometric measurements are represented as *symbols* (some of them have been omitted for clarity), and the *lines* correspond to the fittings using a Tauc–Lorentz dispersion model for a nanometric Bi_2O_3 thin film

of many polarizable atoms with bound electrons that respond to the excitation with light as oscillators.
- The Drude model that takes into account the absorption from free electrons.
- The Lorentz–Drude model where both bound and free electrons are considered.
- The Sellmeier model which corresponds to the Lorentz model when the imaginary dielectric function (or the extinction coefficient) approaches to zero.
- The Cauchy model, which is an approximate function of the Sellmeier model obtained by doing a series expansion of the Sellmeier function.
- The Tauc–Lorentz model which was proposed for amorphous semiconductors but nowadays has also been used for conductive oxide semiconductors and nanocrystalline semiconductors (Jellison and Modine 1996; Chen and Shen 2005). Their formula uses a combination of the Tauc band edge and the Lorentz formulation for a collection of uncoupled atoms to determine the imaginary part of the dielectric function, given by

$$\varepsilon_2(E) = \begin{cases} \dfrac{AE_oC\left(E - E_g\right)^2}{\left[\left(E^2 - E_o^2\right)^2 + C^2E^2\right]}\dfrac{1}{E} & E > E_g \\ 0 & E \le E_g \end{cases} \tag{4.21}$$

The real part is determined using Kramers–Kronig integration (Fujiwara 2007) from zero to infinite.

$$\varepsilon_1(E) = n^2(E) - k^2(E) = \varepsilon_1(\infty) + \frac{2}{\pi}P\int_{E_g}^{\infty}\frac{\xi\varepsilon_2(E)}{\xi^2 - E^2}\mathrm{d}\xi \tag{4.22}$$

where P stands for the Cauchy principal part of the integral and an additional parameter $\varepsilon_1(\infty)$ is also included. Normally, $\varepsilon_1(\infty) = 1$, but it can be greater than 1 if there are significant optical transitions at energies greater than those sampled by the ellipsometer.

- Other models have also been defined for specific classes of materials.

For all of them, the film thickness and the $n(E)$ and $k(E)$ relationships in the spectral range are obtained, as shown in Fig. 4.21 for the same Bi_2O_3 film shown in Fig. 4.20.

Then, the optical gap can be calculated using some of the equations shown in Sect. 4.5. However, as shown in Fig. 4.22a–c the selection of the adequate equation requires previous knowledge about the structure (crystalline or amorphous) and the band structure (direct or indirect gap). Otherwise, any of the models can be applied and a linear region can be used to fit the plot, but the optical gap is completely different according to the model used, as shown in Fig. 4.22a–c, where the gap changes from 3.4 eV assuming a direct gap to 1.55 eV for indirect gap calculation

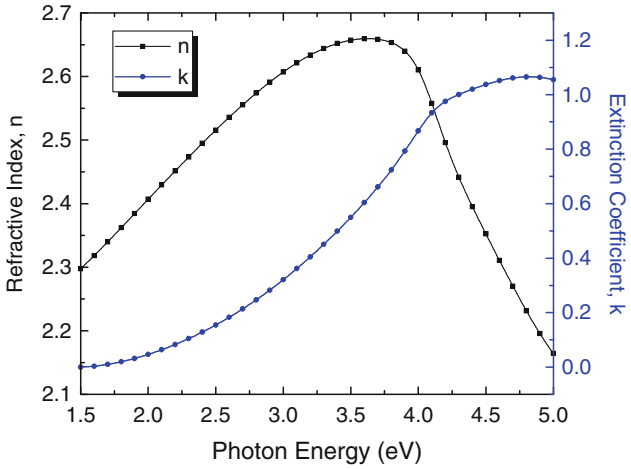

Fig. 4.21 Optical properties obtained for the Bi_2O_3 thin film using the Tauc–Lorentz model

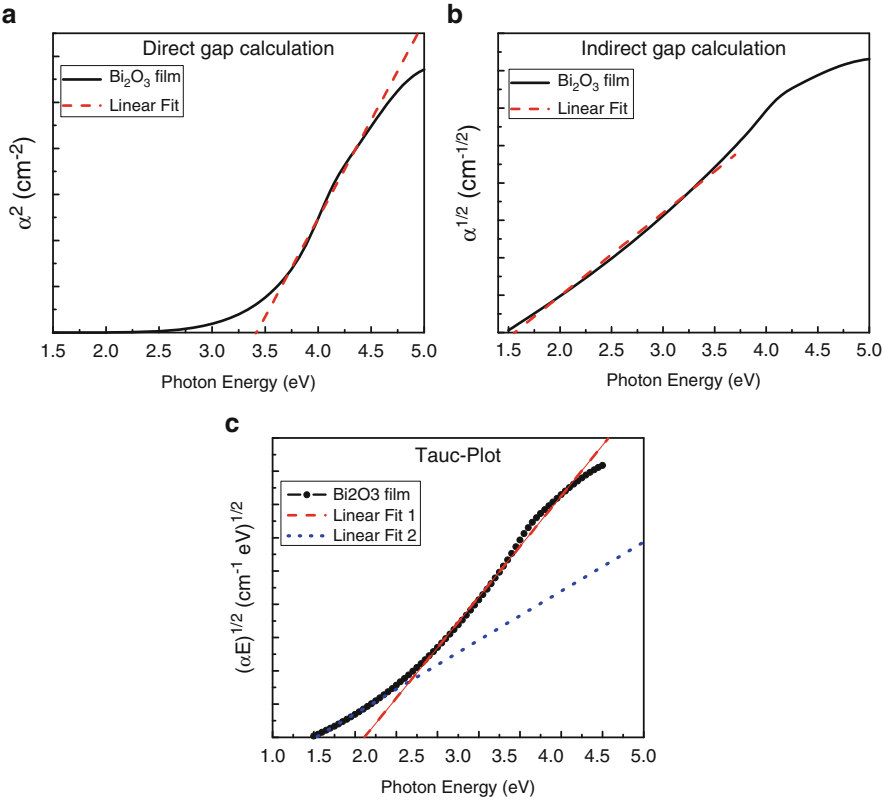

Fig. 4.22 Calculations of the optical band gap for the Bi_2O_3 thin films. (**a**) Using the direct gap model, (**b**) using the indirect gap model, and (**c**) using the Tauc-plot

and assuming amorphous semiconductor, the estimated gap depends strongly in the linear region choose to fit the spectra (2.1 or 1.5 eV), since not a good linear relationship is observed.

Spectroscopic ellipsometry can also provide other electronic and structural parameters. Using appropriate models and analyzing the fitting parameters, information about the energy for inter-/intraband transitions can be obtained, as well as parameters, such as porosity, volume fraction of a second phase, roughness, etc. There is also the capability to perform in situ analysis due to the fast acquisition instrumentation.

4.5.4 Photoluminescence (PL) Spectroscopy

Photoluminsecence spectroscopy is a complimentary technique to UV–VIS DRS in that it also gives information on the electronic structure from light excitation. Whereas UV–VIS DRS looks at the transition from the ground state to the excited state, photoluminescence (PL) spectroscopy differs by examining the transition from the excited state to the ground state. The emission of photons from this phenomenon can be measured as fluorescence. This process is relevant to the study of photocatalysts since fluorescence occurs when electrons in the conduction band recombine with holes in the valence band. Thus, this characterization technique can give direct information on electron transfer kinetics during the photocatalytic process. The PL intensity can be used to compare recombination rates for different photocatalytic systems, detect impurities and defects in the sample, and estimate the band gap through the band to band transitions (Anpo et al. 2009; Gilliand 1997), as it is shown in Fig. 4.23 for a photocatalytic ZnO film. The peak centered at 383 nm corresponds to the band gap of the material (3.23 eV), and the broad band centered at 495 nm indicates a very large number of defects and intrinsic impurities of the ZnO lattice. Moreover, surface species can have a large effect on the PL spectra since surface sites and the presence of adsorbed surface molecules can act as efficient electron traps which help to decrease PL intensity, preventing electron–hole recombination (Anpo et al. 2009; Anpo and Kamat 2010).

The band diagram corresponding to the photoluminescence process in a direct or an indirect gap material is similar to the one given in Fig. 4.15; the only difference is that the arrows point in the opposite direction. Photons are absorbed from an excitation source such as laser of lamp, and this injects electrons into the conduction band and holes into the valence band. This will be possible if the energy of the source $h\nu_L$ is greater than E_g (usually UV light is needed). The electrons can be initially created in states high up in the conduction band, but they do not remain in those states for very long. They rapidly ($\sim 10^{-13}$ s) lose their energy by emitting phonons to satisfy the conservation laws. After the electrons and holes have relaxed as far as they can by phonon emission, they must wait at the bottom of the bands until they can emit a photon or recombine non-radiatively. In Fig. 4.24 the PL

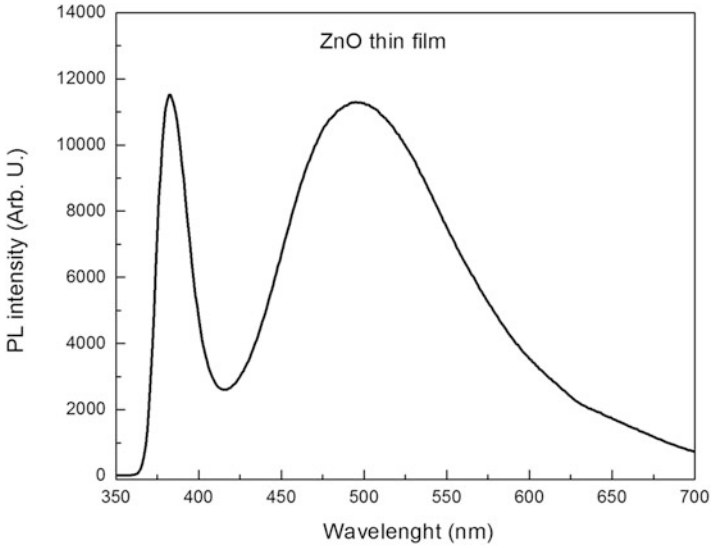

Fig. 4.23 PL spectrum of a photocatalytic ZnO thin film. The peak centered at 383 nm corresponds to the band to band transition ($E_g = 3.23$ eV)

spectra of undoped and Cu-doped photocatalytic ZnS films are shown, where a very broad band in the visible region is observed. The maximum of each band varies within 561 and 599 nm, and the peaks become wider as the Cu concentration increases. These wide bands give orange-red emissions that are a consequence of the overlapping of at least two peaks, one that corresponds to Cu centers—formed if the Zn site is replaced by a Cu^+ ion—(Khomchenko et al. 2005) and the low energy peak that is caused by interstitial Zn and S, which are deep defects that decay in the red region of the spectrum (Chauhan et al. 2013, 2014). The systematic red shift of the band confirms the presence of Cu^{2+} ions in the ZnS matrix (Muthukumaran and Kumar 2013). The highest photocatalytic activity was achieved for the sample with 12 at.% Cu; this amount of impurities provided enough localized states to facilitate the electron transport to the conduction band for the photocatalytic process without compromising it with the radiative recombination.

Time-resolved picosecond in situ PL (TR-PL) spectroscopy is often utilized to examine the recombination lifetimes of electron/hole pairs. Whereas conventional or steady-state PL spectroscopy uses continuous excitation from a light source, TR-PL spectroscopy relies on pulsed excitation and measures photoluminescence at certain time intervals after the pulse excitation (Gilliand 1997; Matsuoka et al. 2008). The PL emission intensity over time is then fitted to an exponential decay model to determine the lifetimes of photogenerated electron/hole pairs (Selby et al. 2003; Quickenden et al. 1996). An increased lifetime of photogenerated electron/hole pairs has been shown to correlate with TiO_2 for photocatalytic splitting (Tang et al. 2008).

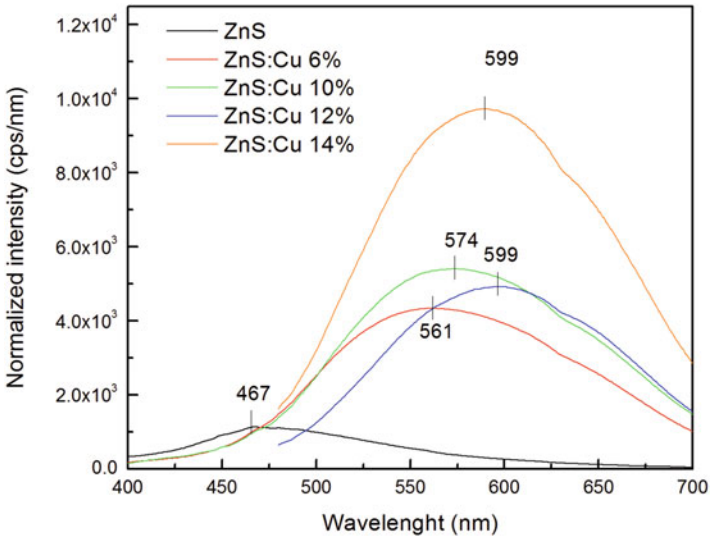

Fig. 4.24 PL spectra of undoped and Cu-doped ZnS photocatalytic films. The highest photocatalytic performance was achieved with ZnO:Cu 12 %, where the PL was not the most intense

4.5.5 Other Methods

As mentioned briefly above, the low energy region of the EEL spectra, less than 50 eV, contains information about the excitation of valence band electrons, such as interband transition (single excitation) and plasmon excitation (collective excitation), and can be used to obtain the local electronic and optical properties of materials at the nanoscale. This technique is called valence electron energy loss spectroscopy (VEELS). The other advantage of the TEM–VEELS method compared to the optical spectroscopies is the wider energy range (~0 to 50 eV). However, the disadvantage is the difficulty of implementation and data analysis that demands the proper substraction of the zero-loss signal.

Similarly, ultraviolet photoelectron spectroscopy, UPS, described qualitatively in Fig. 4.3, used ultraviolet light to ionize valence band electrons, and so the Fermi level and other electronic transition can be determined.

4.5.6 Examples

The band gap determination in a photocatalyst is of primary interest, especially if visible light absorption is pursued. Modifications in the synthesis of a photocatalyst can lead to a decrease in the band gap. The most common way to affect the band gap of semiconductors is by means of doping. This is the case of TiO_2 that has been

doped with F, N, C, etc. (Maeda and Watanabe 2006; Abadias et al. 2010) resulting in smaller band gaps when the proper amount of doping element is incorporated. For thin films the transmittance spectra are usually measured, while for nanopowders or nontransparent samples, the diffuse reflectance is more adequate. Li et al. (2005) reported the effect of N-doped, F-doped, and N–F-codoped TiO_2 powders. The UV–Vis absorption spectra of the compounds were measured, and a clear difference in the absorption edge was observed, where the samples doped with N and codoped with N–F presented an absorption band in the visible range of 400–550 nm. Similarly, impurities of copper in the ZnS semiconductor show a diminution of the band gap from 3.4 to 3.2 eV.

Finally, the high sensitivity of the spectroscopy ellipsometry to detect small changes in the refractive index was investigated by Carretero-Genevrier et al. (2012) that measured the in situ photodegradation of organic species by TiO_2 nanoparticles during UV irradiation. The changes in the refractive index of a different series of layers were measured as a function of the irradiation time. Such changes were then correlated to the nanostructure of the samples, previously studied by GISAXS. Not much experimental details are given about the ellipsometric measurements, as well as concerning the models used. However, it is the proposal for an interesting field of research.

Concluding Remarks

In this chapter we presented an overview of the most important techniques used in the characterization of photocatalytic materials, going from the composition to the structure and properties of the materials. A brief description of each technique was presented in order to provide the physical aspects involved during the use of each one and the information that can be extracted from them. In the examples provided, we pointed the importance of using a combination of several techniques to obtain a better knowledge of the materials under study, especially in the case of complex materials, where independent results or isolated techniques cannot give concluding information of the samples. The proper choice of a number of characterization techniques will allow a better understanding of the properties of the photocatalyst under study.

Acknowledgements Funding from the BisNano project (European Community Seven Framework rogramme and CONACYT under grant agreements n° 263878 and 125141, respectively) and the Phoscleen IRSES project 318977.

References

Abadias G, Paumier F, Eyidi D, Guerin P, Girardeau T (2010) Structure and properties of nitrogen-doped titanium dioxide thin films produced by reactive magnetron sputtering. Surf Interface Anal 42:970–973

Ahmad M, Ahmed E, Hong ZL, Ahmed W, Elhissi A, Khalid NR (2013) Photocatalytic, sonocatalytic and sonophotocatalytic degradation of Rhodamine B using ZnO/CNTs composites photocatalysts. Ultrason Sonochem 21:761–773

Amelinckx S, Van-Dyck D, Van-Landuyt J, Van-Tendeloo G (2008) Electron microscopy: principles and fundamentals. Wiley, Weinheim. ISBN 978-3-527-61455-4

Anpo M, Kamat PV (eds) (2010) Environmentally benign photocatalysts: applications of titanium oxide-based materials. Springer, New York

Anpo M, Dzwigaj S, Che M (2009) Chapter 1: Applications of photoluminescence spectroscopy to the investigation of oxide-containing catalysts in the working state. In: Gates BC, Jentoft FC (eds) Advances in catalysis, vol 52. Elsevier, Amsterdam, pp 1–42

Balaji S, Djaoued Y, Robichaud J (2006) Phonon confinement studies in nanocrystalline anatase-TiO_2 thin films by micro Raman spectroscopy. J Raman Spectrosc 37:1416–1422

Barrett EP, Joyner LG, Halenda PP (1951) The determination of pore volume and area distributions in porous substances. I. Computations from nitrogen isotherms. J Am Chem Soc 73:373–380

Beuvier T, Richard-Plouet M, Brohan L (2009) Accurate methods for quantifying the relative ratio of anatase and TiO_2(B) nanoparticles. J Phys Chem C 113:13703–13706

Briggs D, Sheah MP (1990) Practical surface analysis by Auger and X-ray photoelectron spectroscopy. Wiley, New York

Briggs D, Sheah MP (1996) Ion and neutral spectroscopy. Wiley, New York

Brunauer S, Emmett PH, Teller E (1938) Adsorption of gases in multimolecular layers. J Am Chem Soc 60:309–319

Bunker G (2010) Introduction to XAFS: a practical guide to X-ray absorption fine structure spectroscopy. Cambridge University Press, Cambridge. ISBN 978-0-521-76775-0

Carretero-Genevrier A, Boissiere C, Nicole L, Grosso D (2012) Distance dependence of the photocatalytic efficiency of TiO_2 revealed by in situ ellipsometry. J Am Chem Soc 134:10761–10764

Catlow CRA, Guo ZX, Miskufova M, Shevlin SA, Smith AGH, Sokol AA, Walsh A, Wilson DJ, Woodley SM (2010) Advances in computational studies of energy materials. Philos Trans R Soc A 368:3379–3456

Chauhan R, Kumar A, Chaudhary RP (2013) Photocatalytic degradation of methylene blue with Fe doped ZnS nanoparticles. Spectrochim Acta A 113:250–256

Chauhan R, Kumar A, Chaudhary RP (2014) Photocatalytic degradation of methylene blue with Cu doped ZnS nanoparticles. J Lumin 145:6–13

Chen H, Shen WZ (2005) Perspectives in the characteristics and applications of Tauc-Lorentz dielectric function model. Eur Phys J B 43:503–507

Chipera SJ, Bish DL (2002) FULLPAT: a full-pattern quantitative analysis program for X-ray powder diffraction. International Union of Crystallography, Commission on Powder Diffraction Newsletter, vol 27. pp 27–28.

Chipera SJ, Bish DL (2013) Fitting full X-ray diffraction patterns for quantitative analysis: a method for readily quantifying crystalline and disordered phases. Adv Mater Phys Chem 3:47–53

Chung FH (1974) Quantitative interpretation of X-ray diffraction patterns of mixtures. I. Matrix-flushing method for quantitative multicomponent analysis. J Appl Crystallogr 7:519–525

Cody GD, Brooks BG, Abeles B (1982) Optical absorption above the optical gap of amorphous silicon hydride. Sol Energy Mater 8:231–240

Condon JB (2006) Surface area and porosity determination by physisorption: measurement and theory. Elsevier, Amsterdam. ISBN 978-0-444-51964-1

Dante RC, Martín-Ramos P, Sánchez-Arévalo FM, Huerta L, Bizarro M, Navas-Gracia LM, Martín-Gil J (2013) Synthesis of crumpled nanosheets of polymeric carbon nitride from melamine cyanurate. J Solid State Chem 201:153–163

Davis LE (1996) Handbook of Auger electron spectroscopy physical electronics. A reference book of standard data for identification and interpretation of Auger electron spectroscopy data. Physical Electronics, Eden Prairie, MN

Delgass WN, Haller G, Kellerman RK, Lunsford JH (1979) Spectroscopy in heterogeneous catalysis. Elsevier, Amsterdam. ISBN 978-0-12-210150-2

Deng Q, Duan X, Ng DHL, Tang H, Yang Y, Kong M, Wu Z, Cai W, Wang G (2012) Ag nanoparticle decorated nanoporous ZnO microrods and their enhanced photocatalytic activities. ACS Appl Mater Interfaces 4:6030–6037

Dombrowski RJ, Lastoskie CM, Hyduke DR (2001) The Horvath–Kawazoe method revisited. Colloids Surf A 187–188:23–39

Eaton P, West P (2010) Atomic force microscopy. Oxford University Press, Oxford. ISBN 978-0-19-957045-4

Egerton RF (2011) Electron energy-loss spectroscopy in the electron microscope, 3rd edn. Springer, New York. ISBN 978-1-4419-9583-4

Fagerlund G (1973) Determination of specific surface by the BET method. Matériaux et Construction 6:239–245

Ferraro J, Nakamoto K, Brown CW (2003) Introductory Raman spectroscopy. Elsevier, Amsterdam. ISBN 978-0-12-254105-6

Fox M (2010) Optical properties of solids. Oxford University Press, Oxford. ISBN 10: 0199573379

Froitzheim H (1977) Electron energy loss spectroscopy. In: Ibach H (ed) Electron spectroscopy for surface analysis, vol 4. Springer, Berlin, pp 205–250

Fujiwara H (2007) Spectroscopy ellipsometry; principle and applications. Wiley, West Sussex. ISBN 9780470016084

Gauden PA, Terzyk AP, Rychlicki G, Kowalczyk P, Cwiertnia MS, Garbacz JK (2004) Estimating the pore size distribution of activated carbons from adsorption data of different adsorbates by various methods. J Colloid Interface Sci 273:39–63

Gilliand GD (1997) Photoluminescence spectroscopy of crystalline semiconductors. Mater Sci Eng R 18:99–399

Glatter VO, Kratky O (1982) Small angle X-ray scattering. Academic, London. ISBN 0-12-286280-5

Goldstein JI, Newbury DE, Echlin P, Joy DC, Lyman CE, Lifshin E, Sawyer L, Michael JR (2003) Scanning electron microscopy and X-ray microanalysis . Kluwer-Plenum, New York. ISBN 0-306-47292-9

Goodhew PJ, Humphreys J, Beanland R (2000) Electron microscopy and analysis, 3rd edn. Taylor & Francis, London. ISBN 0-7484-0968-8

Gualtieri AF (2000) Accuracy of XRPD QPA using the combined Rietveld and RIR method. J Appl Crystallogr 33:267–278

Guillén C, Montero J, Herrero J (2014) Anatase and rutile TiO_2 thin films prepared by reactive DC sputtering at high deposition rates on glass and flexible polyimide substrates. J Mater Sci 49:5035–5042

Hafez HS (2012) Highly active ZnO rod-like nanomaterials: synthesis characterization and photocatalytic activity for dye removal. Physica E Low Dimens Syst Nanostruct 44:1522–1527

Hardcastle FD (2011) Raman spectroscopy of titania (TiO_2) nanotubular water-splitting catalysts. J Ark Acad Sci 65:43–48

Haugstad G (2012) Atomic force microscopy: understanding basic modes and advanced applications. Wiley, Hoboken, NJ. ISBN 978-0-470-63882-8

Haw JF (2002) In situ spectroscopy in heterogeneous catalysis. Wiley-VCH, Weinheim. ISBN 9783527302482

Horvath-Bordon E, Kroke E, Svoboda I, Fuess H, Riedel R, Neeraj S, Cheetham AK (2004) Alkalicyamelurates $M_3[C_6N_7O_3]xH_2O$ M = Li, Na, K, Rb, Cs: UV-luminescent and thermally very stable ionic tri-s-triazine derivatives. Dalton Trans 22:3900–3908

Huang L, Xu H, Zhang R, Cheng X, Xia J, Xu Y, Li H (2013) Synthesis and characterization of g-C_3N_4/MoO_3 photocatalyst with improved visible-light photoactivity. Appl Surf Sci 283:25–32

Jellison GE, Modine FA (1996) Parameterization of the optical functions of amorphous materials in the interband region. Appl Phys Lett 69:371–373

Johansson SAE, Campbell JL, Malqvist KG (eds) (1995) Particle induced X-ray emission spectrometry (PIXE). Wiley, Chichester. ISBN 978-0-471-58944-0

Keast VJ, Scott AJ, Brydson R, Williams DB, Bruley J (2001) Electron energy-loss near-edge structure—a tool for the investigation of electronic structure on the nanometre scale. J Microsc 203:135–175

Khomchenko V, Fedorenko L, Yusupov N, Rodionov V, Bacherikov Y, Svechnikov G, Zavyalova L, Roshchina N, Lytvyn P, Mukhlio M (2005) Laser processing and characterization of ZnS Cu thin films. Appl Surf Sci 247:434–439

Kowalczyk P, Terzyk AP, Gauden PA, Leboda R, Szmechtig-Gauden E, Rychlicki G, Ryu Z, Rong H (2003) Estimation of the pore-size distribution function from the nitrogen adsorption isotherm. Comparison of density functional theory and the method of Do and co-workers. Carbon 41:1113–1125

Kundu S, Ciston J, Senanayake SD, Arena DA, Fujita E, Stacchiola D, Barrio L, Navarro RM, Fierro JLG, Rodriguez JA (2012) Exploring the structural and electronic properties of Pt/Ceria-modified TiO_2 and its photocatalytic activity for water splitting under visible light. J Phys Chem C 116:14062–14070

Kuzmany H (2010) Solid-state spectroscopy: an introduction. Springer, Berlin. ISBN 978-3-642-01479-6

Lai Y, Meng M, Yu Y (2010) One-step synthesis, characterizations and mechanistic study of nanosheets-constructed fluffy ZnO and Ag/ZnO spheres used for Rhodamine B photodegradation. Appl Catal B Environ 100:491–501

Lamberti C, Zecchina A, Groppo E, Bordiga S (2010) Probing the surfaces of heterogeneous catalysts by in situ IR spectroscopy. Chem Soc Rev 39:4951–5001

Lastoskie CM, Gubbins KE (2000) Characterization of porous materials using density functional theory and molecular simulation. Stud Surf Sci Catal 128:41–50

Li X, He J (2013) Synthesis of raspberry-like SiO_2-TiO_2 nanoparticles toward antireflective and self-cleaning coatings. ACS Appl Mater Interfaces 5:5282–5290

Li D, Ohashi N, Hishita S, Kolodiazhnyi T, Haneda H (2005) Origin of visible-light-driven photocatalysis: a comparative study on N/F-doped and N–F-codoped TiO_2 powders by means of experimental characterizations and theoretical calculations. J Solid State Chem 178:3293–3302

Li G, Zhang D, Yu JC (2009) Thermally stable ordered mesoporous CeO_2/TiO_2 visible-light photocatalysts. Phys Chem Chem Phys 11:3775–3782

Liang Q, Shi Y, Ma W, Li Z, Yang X (2012) Enhanced photocatalytic activity and structural stability by hybridizing Ag_3PO_4 nanospheres with graphene oxide sheets. Phys Chem Chem Phys 14:15657–15665

Lin D, Wu H, Zhang R, Pan W (2009) Enhanced photocatalysis of electrospun Ag–ZnO heterostructured nanofibers. Chem Mater 21:3479–3484

Liu H, Ji S, Zheng Y, Li M, Yang H (2013a) Porous TiO_2-coated magnetic core-shell nanocomposites: preparation and enhanced photocatalytic activity. Chin J Chem Eng 21:569–576

Liu L, Bai H, Liu J, Sun DD (2013b) Multifunctional graphene oxide-TiO_2-Ag nanocomposites for high performance water disinfection and decontamination under solar irradiation. J Hazard Mater 261C:214–223

Lowell S, Shields JE (1984) Powder surface area and porosity, Powder Technology Series. Springer, Berlin. ISBN 978-94-010-8953-1

Lowell S, Shields JE, Thomas MA, Thommes M (2004) Characterization of porous solids and powders: surface area, pore size and density. Springer, Berlin. ISBN 1402023022

Maeda M, Watanabe T (2006) Visible light photocatalysis of nitrogen-doped titanium oxide films prepared by plasma-enhanced chemical vapor deposition. J Electrochem Soc 153:C186–C189

Matsuoka M, Kamegawa T, Anpo M (2008) Photoluminescence spectroscopy an its application to the characterization of active sites and reaction dynamics in catalysis. In: Ertl G, Knézinger H, Schiith F, Weitkamp J (eds) Handbook of heterogeneous catalysis. Wiley, Weinheim, pp 1065–1073

McDermott EJ, Wirnhier E, Schnick W, Virdi KS, Scheu C, Kauffmann Y, Kaplan WD, Kurmaev EZ, Moewes A (2013) Band gap tuning in poly(triazine imide), a nonmetallic photocatalyst. J Phys Chem C 117:8806–8812

Moria S, Wiesendanger R, Meyer E (2002) Noncontact atomic force microscopy. Springer, New York

Moser EM, Chappuis S, Olleros J (2013) Production of photocatalytically active titania layers: a comparison of plasma processes and coating properties. Surf Coat Technol 227:2–9

Murphy AB (2006) Modified Kubelka–Munk model for calculation of the reflectance of coatings with optically-rough surfaces. J Phys D Appl Phys 39:3571–3581

Murphy AB (2007a) Band gap determination from diffuse reflectance measurements of semiconductor films, and application to photoelectrochemical water-splitting. Sol Energy Mater Sol Cells 91:1326–1337

Murphy AB (2007b) Optical properties of an optically rough coating from inversion of diffuse reflectance measurements. Appl Opt 46:3133–3143

Muthukumaran S, Kumar MA (2013) Structural, FTIR and photoluminescence properties of ZnS: Cu thin films by chemical bath deposition method. Mater Lett 93:223–225

Qi B, Yu Y, He X, Wu L, Duan X, Zhi J (2012) Series of transition metal-doped TiO_2 transparent aqueous sols with visible-light response. Mater Chem Phys 135:549–553

Quickenden TI, Green TA, Lennon D (1996) Luminescence from UV-Irradiated Amorphous H2O Ice. J Phys Chem 100:16801

Reimer L, Kohl H (2008) Transmission electron microscopy. Springer, Berlin. ISBN 978-0-387-40093-8

Rengifo-Herrera JA, Mielczarski E, Mielczarski J, Castillo NC, Kiwi J, Pulgarin C (2008) Escherichia coli inactivation by N, S co-doped commercial TiO_2 powders under UV and visible light. Appl Catal Environ 84:448–456

Rietveld HM (1969) A profile refinement method for nuclear and magnetic structures. J Appl Crystallogr 2(2):65–71

Rouquerol F, Rouquerol J, Sing KSW, Llewellyn P, Maurin G (2014) Adsorption by powders and porous solids. Principles, methodology and applications. Academic, Oxford. ISBN 978-0-08-097035-6

Schartl W (2007) Light scattering from polymer solutions and nanoparticle dispersions. Springer, New York. ISBN 978-3-540-71951-9

Schiettekatte F, Chicoine M, Forster J.S, Geiger J.S, Gujrathi S, Kolarova R, Paradis A, Roorda S, Wei P (2004) Nuclear Instruments and Methods in Physics Research B ERD,15 N external beam for NRRA in air, HIRBS: ion beam analysis developments on the HVEC EN1 Tandem 219–220:430–434

Selby BJ, Quickenden TI, Freeman CG (2003) The fitting of luminescence rises and decays. Kinet Catal 44:5–15

Sério S, Melo Jorge ME, Nunes Y, Barradas NP, Alves E, Munnik F (2012) Incorporation of N in TiO_2 films grown by DC-reactive magnetron sputtering. Nucl Instrum Methods Phys Res B 273:109–112

Siketic Z, Radovic IB, Jaksic M, Skukan N (2010) Time of flight elastic recoil detection analysis with a position sensitive detector. Rev Sci Instrum 81:033305

Sing KSW (1985) Reporting physisorption data for gas/solid systems with special reference to the determination of surface area and porosity. Pure Appl Chem 54:2201–2218
Sridharan K, Jang E, Park TJ (2013) Novel visible light active graphitic C_3N_4–TiO_2 composite photocatalyst: synergistic synthesis, growth and photocatalytic treatment of hazardous pollutants. Appl Catal B Environ 142–143:718–728
Stohr J (2003) NEXAFS spectroscopy. Springer, Berlin. ISBN 3-540-54422-4
Suryanarayana C, Norton MG (1998) X-ray diffraction: a practical approach. Springer, New York. ISBN 978-1-4899-0148-4
Swamy V, Kuznetsov A, Dubrovinsky LS, Caruso RA, Shchukin DG, Muddle BC (2005) Finite-size and pressure effects on the Raman spectrum of nanocrystalline anatase TiO_2. Phys Rev B 71:184302
Tang J, Durrant JR, Klug DR (2008) J Am Chem Soc 130:13885
Tauc J, Grigorovici R, Vancu A (1966) Optical properties and electronic structure of amorphous germanium. Phys Status Solidi B 15:627–637
Tavares CJ, Marques SM, Viseu T, Teixeira V, Carneiro JO, Alves E, Barradas NP, Munnik F, Girardeau T, Rivière J-P (2009) Enhancement in the photocatalytic nature of nitrogen-doped PVD-grown titanium dioxide thin films. J Appl Phys 106:113535
Tesmer JR, Nastasi MA (1995) Handbook of modern ion beam analysis. Materials Research Society, Pittsburgh. http://www.quantachrome.com/technotes.html
Thommes M. Pore size analysis by gas adsorption. Part I: Aspects of the application of Density Functional Theory (DFT) and Monte Carlo simulation (MC) for micro/mesopore size analysis. Quantachrome Instruments, Technical & Application Notes N. 31, pp. 1–7
Tompkins HG, Irene EA (2005) Handbook of ellipsometry. William Andrew, Norwich, NY. ISBN 0-8155-1499-9
Ulyanenkov A (1998) Grazing-incidence X-ray diffraction from multilayers taking into account diffuse scattering from rough interfaces. Appl Phys A 66:193–199
Wang S, Liu S, Guo J, Guo Q (2013) Surface electronic structure and morphology of silver on iron oxide films. Surf Sci 607:124–129
Waseda Y, Matsubara E, Shinoda K (2011) X-ray diffraction crystallography: introduction, examples and solved problems. Springer, Berlin. ISBN 978-3-642-16635-8
Watts JF, Wolstenholme J (2003) An introduction to surface analysis by XPS and AES. Wiley, New York. ISBN 978-0-470-84713-8
Weckhuysen BM, Vand Der Voort P, Catana G (2000) Spectroscopy of transition metal ions on surfaces. Leuven University Press, Leuven. ISBN 90-5867-025-2
Williams DDB, Carter CB (1996) Transmission electron microscopy: a textbook for materials science. Plenum Press, New York
Xie J, Jiang D, Chen M, Li D, Zhu J, Lü X, Yan C (2010) Preparation and characterization of monodisperse Ce-doped TiO_2 microspheres with visible light photocatalytic activity. Colloids Surf A 372:107–114
Xu M, Gao Y, Moreno EM, Kunst M, Muhler M, Wang Y, Idriss H, Wöll C (2011) Photocatalytic activity of bulk TiO_2 anatase and rutile single crystals using infrared absorption spectroscopy. Phys Rev Lett 106:138302
Yan SC, Li ZS, Zou ZG (2009) Photodegradation performance of g-C_3N_4 fabricated by directly heating melamine. Langmuir 25:10397–10401
Zhu M, Li Z, Xiao B, Lu Y, Du Y, Yang P, Wang X (2013) Surfactant assistance in improvement of photocatalytic hydrogen production with the porphyrin noncovalently functionalized graphene nanocomposite. ACS Appl Mater Interfaces 5:1732–1740